

Interferometric Near-Infrared Spectroscopy (iNIRS) for determination of optical and dynamical properties of turbid media

Dawid Borycki,^{1,2} Oybek Kholiqov,¹ Shau Poh Chong,¹
and Vivek J. Srinivasan^{1,*}

¹Biomedical Engineering Department, University of California Davis, Davis, CA 95616, USA

²Institute of Physics, Faculty of Physics, Astronomy and Informatics, Nicolaus Copernicus University, Grudziadzka 5, 87-100 Torun, Poland

*vjsriniv@ucdavis.edu

Abstract: We introduce and implement interferometric near-infrared spectroscopy (iNIRS), which simultaneously extracts optical and dynamical properties of turbid media through analysis of a spectral interference fringe pattern. The spectral interference fringe pattern is measured using a Mach-Zehnder interferometer with a frequency-swept narrow linewidth laser. Fourier analysis of the detected signal is used to determine time-of-flight (TOF)-resolved intensity, which is then analyzed over time to yield TOF-resolved intensity autocorrelations. This approach enables quantification of optical properties, which is not possible in conventional, continuous-wave near-infrared spectroscopy (NIRS). Furthermore, iNIRS quantifies scatterer motion based on TOF-resolved autocorrelations, which is a feature inaccessible by well-established diffuse correlation spectroscopy (DCS) techniques. We prove this by determining TOF-resolved intensity and temporal autocorrelations for light transmitted through diffusive fluid phantoms with optical thicknesses of up to 55 reduced mean free paths (approximately 120 scattering events). The TOF-resolved intensity is used to determine optical properties with time-resolved diffusion theory, while the TOF-resolved intensity autocorrelations are used to determine dynamics with diffusing wave spectroscopy. iNIRS advances the capabilities of diffuse optical methods and is suitable for *in vivo* tissue characterization. Moreover, iNIRS combines NIRS and DCS capabilities into a single modality.

© 2016 Optical Society of America

OCIS codes: (110.4153) Motion estimation and optical flow; (160.4760) Optical properties; (290.1990) Diffusion; (290.4210) Multiple scattering; (290.7050) Turbid media; (030.1640) Coherence.

References and links

1. F. Jobsis, "Noninvasive, infrared monitoring of cerebral and myocardial oxygen sufficiency and circulatory parameters," *Science* **198**, 1264–1267 (1977).
2. A. Torricelli, D. Contini, A. Pifferi, M. Caffini, R. Re, L. Zucchelli, and L. Spinelli, "Time domain functional NIRS imaging for human brain mapping," *Neuroimage* **85**, 28–50 (2014).
3. F. Scholkmann, S. Kleiser, A. J. Metz, R. Zimmermann, J. M. Pavia, U. Wolf, and M. Wolf, "A review on continuous wave functional near-infrared spectroscopy and imaging instrumentation and methodology," *Neuroimage* **85**, 6–27 (2014).

4. T. Durduran and A. G. Yodh, "Diffuse correlation spectroscopy for non-invasive, micro-vascular cerebral blood flow measurement," *Neuroimage* **85**, 51–63 (2014).
5. M. Ferrari, and V. Quaresima, "A brief review on the history of human functional near-infrared spectroscopy (fNIRS) development and fields of application," *Neuroimage* **63**, 921–935 (2012).
6. P. Katherine, H. Taber, P. Elizabeth, M. C. Hillman, and M. Robin A. Hurley, "Optical imaging: A new window to the adult brain," *The Journal of Neuropsychiatry and Clinical Neurosciences* **22**, 357–360 (2010).
7. M. S. Patterson, B. Chance, and B. C. Wilson, "Time resolved reflectance and transmittance for the noninvasive measurement of tissue optical properties," *Appl. Opt.* **28**, 2331–2336 (1989).
8. D. V. O'Connor and D. Phillips, eds., *Time-Correlated Single Photon Counting* (Academic, 1984).
9. E. Gratton, W. W. Mantulin, M. J. van de Ven, J. Fishkin, M. Maris, and B. Chance, "The possibility of a near-infrared imaging system using frequency-domain methods," in *Proc. Third Int. Conf. on Peace Through Mind/Brain Science*, (Hamamatsu, 1990), p. 193.
10. J. B. Fishkin and E. Gratton, "Propagation of photon-density waves in strongly scattering media containing an absorbing semi-infinite plane bounded by a straight edge," *J. Opt. Soc. Am. A* **10**, 127–140 (1993).
11. S. Fantini, M. A. Franceschini, J. B. Fishkin, B. Barbieri, and E. Gratton, "Quantitative determination of the absorption spectra of chromophores in strongly scattering media: a light-emitting-diode based technique," *Appl. Opt.* **33**, 5204–5213 (1994).
12. B. J. Berne and R. Pecora, *Dynamic Light Scattering with Applications to Chemistry, Biology, and Physics* (Dover Publications, 2000).
13. G. Maret and P. E. Wolf, "Multiple light scattering from disordered media. The effect of brownian motion of scatterers," *Z. Phys. B: Condens. Matter* **65**, 409 (1987).
14. D. J. Pine, D. A. Weitz, P. M. Chaikin, and E. Herbolzheimer, "Diffusing wave spectroscopy," *Phys. Rev. Lett.* **60**, 1134–1137 (1988).
15. M. J. Stephen, "Temporal fluctuations in wave propagation in random media," *Phys. Rev. B* **37**, 1–5 (1988).
16. F. C. MacKintosh and S. John, "Diffusing-wave spectroscopy and multiple scattering of light in correlated random media," *Phys. Rev. B* **40**, 2383–2406 (1989).
17. D. A. Boas, L. E. Campbell, and A. G. Yodh, "Scattering and imaging with diffusing temporal field correlations," *Phys. Rev. Lett.* **75**, 1855–1858 (1995).
18. A. G. Yodh, P. D. Kaplan, and D. J. Pine, "Pulsed diffusing-wave spectroscopy: High resolution through nonlinear optical gating," *Phys. Rev. B* **42**, 4744–4747 (1990).
19. D. A. Boas and A. K. Dunn, "Laser speckle contrast imaging in biomedical optics," *J. Biomed. Opt.* **15**, 011109 (2010).
20. P.-A. Lemieux and D. J. Durian, "Investigating non-gaussian scattering processes by using nth-order intensity correlation functions," *J. Opt. Soc. Am. A* **16**, 1651–1664 (1999).
21. B. Ackerson, R. Dougherty, N. Reguigui, and U. Nobbman, "Correlation transfer: application of radiative transfer solution methods to photon correlation problems," *J. Thermophys. Heat Transf.* **6**, 577 (1992).
22. D. A. Boas and A. G. Yodh, "Spatially varying dynamical properties of turbid media probed with diffusing temporal light correlation," *J. Opt. Soc. Am. A* **14**, 192–215 (1997).
23. T. Durduran, R. Choe, W. B. Baker, and A. G. Yodh, "Diffuse optics for tissue monitoring and tomography," *Rep. Prog. Phys.* **73**, 076701 (2010).
24. M. Heckmeier, S. E. Skipetrov, G. Maret, and R. Maynard, "Imaging of dynamic heterogeneities in multiple-scattering media," *J. Opt. Soc. Am. A* **14**, 185–191 (1997).
25. V. Jain, E. M. Buckley, D. J. Licht, J. M. Lynch, P. J. Schwab, M. Y. Naim, N. A. Lavin, S. C. Nicolson, L. M. Montenegro, A. G. Yodh, and F. W. Wehrli, "Cerebral oxygen metabolism in neonates with congenital heart disease quantified by MRI and optics," *J. Cereb. Blood Flow. Metab.* **34**, 380–388 (2014).
26. N. Roche-Labarbe, A. Fenoglio, H. Radhakrishnan, M. Kocienski-Filip, S. A. Carp, J. Dubb, D. A. Boas, P. E. Grant, and M. A. Franceschini, "Somatosensory evoked changes in cerebral oxygen consumption measured non-invasively in premature neonates," *Neuroimage* **85**, 279–286 (2014).
27. J.-M. Tualle, E. Tinet, and S. Avrillier, "A new and easy way to perform time-resolved measurements of the light scattered by a turbid medium," *Opt. Commun.* **189**, 211–220 (2001).
28. J.-M. Tualle, H. L. Nghiêm, M. Cheikh, D. Etori, E. Tinet, and S. Avrillier, "Time-resolved diffusing wave spectroscopy beyond 300 transport mean free paths," *J. Opt. Soc. Am. A* **23**, 1452–1457 (2006).
29. L. Mei, S. Svanberg, and G. Somesfalean, "Frequency-modulated light scattering in colloidal suspensions," *Appl. Phys. Lett.* **102**, 061104 (2013).
30. L. Mei, G. Somesfalean, and S. Svanberg, "Frequency-modulated light scattering interferometry employed for optical properties and dynamics studies of turbid media," *Biomed. Opt. Express* **5**, 2810–2822 (2014).
31. D. Huang, E. A. Swanson, C. P. Lin, J. S. Schuman, W. G. Stinson, W. Chang, M. R. Hee, T. Flotte, K. Gregory, C. A. Puliafito, and J. G. Fujimoto, "Optical Coherence Tomography," *Science* **254**, 1178–1181 (1991).
32. A. F. Fercher, W. Drexler, C. K. Hitzenberger, and T. Lasser, "Optical coherence tomography – principles and applications," *Rep. Prog. Phys.* **66**, 239 (2003).
33. W. Drexler and J. Fujimoto, eds., *Optical Coherence Tomography. Technology and Applications* (Springer, 2008).
34. M. Wojtkowski, "High-speed optical coherence tomography: basics and applications," *Appl. Opt.* **49**, D30–D61

- (2010).
35. K. Takada, I. Yokohama, K. Chida, and J. Noda, "New measurement system for fault location in optical waveguide devices based on an interferometric technique," *Appl. Opt.* **26**, 1603–1606 (1987).
 36. R. C. Youngquist, S. Carr, and D. E. N. Davies, "Optical coherence-domain reflectometry: a new optical evaluation technique," *Opt. Lett.* **12**, 158–160 (1987).
 37. M. R. Hee, J. A. Izatt, J. M. Jacobson, and J. G. Fujimoto, "Femtosecond transillumination optical coherence tomography," *Opt. Lett.* **18**, 950–952 (1993).
 38. J. A. Izatt, M. R. Hee, G. M. Owen, E. A. Swanson, and J. G. Fujimoto, "Optical coherence microscopy in scattering media," *Opt. Lett.* **19**, 590–592 (1994).
 39. G. Popescu, and A. Dogariu, "Optical path-length spectroscopy of wave propagation in random media," *Opt. Lett.* **24**, 442–444 (1999).
 40. K. K. Bizheva, A. M. Siegel, and D. A. Boas, "Path-length-resolved dynamic light scattering in highly scattering random media: The transition to diffusing wave spectroscopy," *Phys. Rev. E* **58**, 7664 (1988).
 41. J. Kalkman, R. Sprik, and T. G. van Leeuwen, "Path-Length-Resolved Diffusive Particle Dynamics in Spectral-Domain Optical Coherence Tomography," *Phys. Rev. Lett.* **105**, 198302 (2010).
 42. J. M. Schmitt, A. Knüttel, and R. F. Bonner, "Measurement of optical properties of biological tissues by low-coherence reflectometry," *Appl. Opt.* **30**, 6032–6042 (1993).
 43. V. Duc Nguyen, D. J. Faber, E. van der Pol, T. G. van Leeuwen, and J. Kalkman, "Dependent and multiple scattering in transmission and backscattering optical coherence tomography," *Opt. Express* **21**, 29145–29156 (2013).
 44. L. Mandel and E. Wolf, "Coherence properties of optical fields," *Rev. Mod. Phys.* **37**, 231 (1965).
 45. L. Mandel and E. Wolf, *Optical Coherence and Quantum Optics* (Cambridge University, 1995).
 46. M. Born and E. Wolf, *Principles of Optics* (Cambridge University, 1999).
 47. N. Wiener, "Generalized harmonic analysis," *Acta. Math.* **55**, 117 (1930).
 48. A. Khintchine, "Korrelationstheorie der stationären stochastischen prozesse," *Math. Ann.* **109**, 604–615 (1934).
 49. M. Wojtkowski, A. Kowalczyk, R. Leitgeb, and A. F. Fercher, "Full range complex spectral optical coherence tomography technique in eye imaging," *Opt. Lett.* **27**, 1415–1417 (2002).
 50. J. C. Dainty, "Some statistical properties of random speckle patterns in coherent and partially coherent illumination," *Opt. Acta* **17**, 761–772 (1970).
 51. J. W. Goodman, "Some fundamental properties of speckle," *J. Opt. Soc. Am.* **66**, 1145–1150 (1976).
 52. J. W. Goodman, *Speckle Phenomena in Optics. Theory and Applications* (Roberts and Company Publishers, 2006).
 53. R. Bonner and R. Nossal, "Model for laser doppler measurements of blood flow in tissue," *Appl. Opt.* **20**, 2097–2107 (1981).
 54. S. Chandrasekhar, *Radiative Transfer* (Dover, New York, 1960).
 55. A. Ishimaru, *Wave Propagation and Scattering in Random Media* (Academic, 1978).
 56. R. C. Haskell, L. O. Svaasand, T.-T. Tsay, T.-C. Feng, B. J. Tromberg, and M. S. McAdams, "Boundary conditions for the diffusion equation in radiative transfer," *J. Opt. Soc. Am. A* **11**, 2727–2741 (1994).
 57. D. Contini, F. Martelli, and G. Zaccanti, "Photon migration through a turbid slab described by a model based on diffusion approximation. I. Theory," *Appl. Opt.* **36**, 4587–4599 (1997).
 58. D. J. Pine, D. A. Weitz, P. M. Chaikin, and E. Herbolzheimer, "Features of diffusing-wave spectroscopy," in *OSA Proceedings on Photon Correlation Techniques and Applications, Vol. 1*, J. Abbiss and A. E. Smart, eds. (Optical Society of America, 1988), pp. 35–43.
 59. T. E. Matthews, M. Medina, J. R. Maher, H. Levinson, W. J. Brown and A. Wax, "Deep tissue imaging using spectroscopic analysis of multiply scattered light," *Optica* **1**, 105–111 (2014).
 60. L. A. Coldren, S. W. Corzine, and M. L. Mašanović, *Diode Lasers and Photonic Integrated Circuits, 2nd Edition* (John Wiley & Sons, Inc., 2012).
 61. R. Huber, M. Wojtkowski, K. Taira, J. Fujimoto, and K. Hsu, "Amplified, frequency swept lasers for frequency domain reflectometry and OCT imaging: design and scaling principles," *Opt. Express* **13**, 3513–3528 (2005).
 62. S. Venkatesh and W. Sorin, "Phase noise considerations in coherent optical FMCW reflectometry," *J. Lightwave Technol.* **11**, 1694–1700 (1993).
 63. H. Kogelnik and C. V. Shank, "Coupled-wave theory of distributed feedback lasers," *J. Appl. Phys.* **43**, 2327–2335 (1972).
 64. K. M. Yoo, F. Liu, and R. R. Alfano, "When does the diffusion approximation fail to describe photon transport in random media?" *Phys. Rev. Lett.* **64**, 2647–2650 (1990).
 65. R. Michels, F. Foschum, and A. Kienle, "Optical properties of fat emulsions," *Opt. Express* **16**, 5907–5925 (2008).
 66. P. D. Ninni, F. Martelli, and G. Zaccanti, "Intralipid: towards a diffusive reference standard for optical tissue phantoms," *Phys. Med. Biol.* **56**, N21 (2011).
 67. T. Svensson, R. Savo, E. Alerstam, K. Vynck, M. Burreli and D. S. Wiersma, "Exploiting breakdown of the similarity relation for diffuse light transport: simultaneous retrieval of scattering anisotropy and diffusion constant," *Opt. Lett.* **38**, 437–439 (2013).

68. L. Spinelli, M. Botwicz, N. Zolek, M. Kacprzak, D. Milej, P. Sawosz, A. Liebert, U. Weigel, T. Durduran, F. Foschum, A. Kienle, F. Baribeau, S. Leclair, J.-P. Bouchard, I. Noiseux, P. Gallant, O. Mermut, A. Farina, A. Pifferi, A. Torricelli, R. Cubeddu, H.-C. Ho, M. Mazurenka, H. Wabnitz, K. Klauenberg, O. Bodnar, C. Elster, M. Bénazech-Lavoué, Y. Bérubé-Lauzière, F. Lesage, D. Khoptyar, A. A. Subash, S. Andersson-Engels, P. D. Ninni, F. Martelli, and G. Zaccanti, "Determination of reference values for optical properties of liquid phantoms based on intralipid and india ink," *Biomed. Opt. Express* **5**, 2037–2053 (2014).
 69. N. Weiss, T. G. van Leeuwen, and J. Kalkman, "Localized measurement of longitudinal and transverse flow velocities in colloidal suspensions using optical coherence tomography," *Phys. Rev. E* **88**, 042312 (2013)
 70. L. Wang, S. L. Jacques, and L. Zheng, "MCML – Monte Carlo modeling of light transport in multi-layered tissues," *Comput. Methods Programs Biomed.* **47**, 131–146 (1995).
-

1. Introduction

Near-infrared spectroscopy (NIRS) is a portable and noninvasive method of determining optical properties, i.e. the absorption coefficient (μ_a) and reduced scattering coefficient (μ'_s) of highly scattering media [1]. Quantitative measures of μ_a and μ'_s at one or more wavelengths provide information about parameters such as blood oxygenation, tissue composition, and blood volume [2]. Furthermore, NIRS constitutes the basis for tools aimed at monitoring and imaging of cerebral hemodynamics [3, 4], is widely used in neuroscience [5], and has the potential to contribute to diagnosis of neurological conditions [6].

In conventional, continuous-wave (CW) NIRS, optical properties are extracted from near-infrared light intensity attenuation by a turbid medium. However, quantification of optical properties using CW NIRS requires a number of assumptions regarding scattering and path length [3]. Therefore, robust measurement of μ_a and μ'_s typically requires time domain or frequency domain approaches, both of which add an additional dimension to the measurement space. In particular, in time domain (TD) NIRS [2] a near-infrared picosecond light pulse is delivered to the tissue and the reflected optical intensity is analyzed by the detector as a function of time. The resulting temporal signal constitutes the photon distribution of time-of-flight (DTOF). Subsequently, the values of μ_a and μ'_s are determined from temporal features such as the slope and the peak location of the measured DTOF [2, 7]. However, most modern TD NIRS instruments utilize expensive pulsed lasers and complex time-correlated single photon counting detection [8], making widespread adoption of this technology challenging. In frequency domain (FD) NIRS [9–11], the light intensity is sinusoidally modulated before it is delivered to the tissue. Optical properties of the medium are then calculated from the amplitude attenuation and phase shift of the detected wave. Though optical properties can be measured with FD NIRS, the DTOF is typically not directly resolved, and modulation/demodulation schemes can be complex and expensive.

While NIRS methods can determine hemoglobin concentrations and oxygen saturation, blood flow is necessary to relate oximetry to metabolism. The dynamic properties of scatterers [12–18] and blood flow in the retina, skin or brain [4, 19] can be determined from temporal intensity fluctuations of reemitted coherent light. These techniques, which are commonly referred to as diffuse correlation spectroscopy (DCS) or laser speckle flowmetry, measure temporal light intensity autocorrelations to determine flow. In particular, they infer the decay of the optical field autocorrelation, related to blood flow, from the intensity autocorrelation function using the Siegert relation [20]. Subsequently the effective Brownian motion, which is related to blood flow in living tissue [4], is extracted from diffusing wave spectroscopy (DWS) theory [14] or the diffusion correlation equation (DCE) [17, 21–24]. However, there are major downfalls of such an approach. Namely, field autocorrelations, particularly when averaged over photon paths, depend not only on the motion of scatterers but also on the optical properties of the diffusive medium. Thus, DCS analysis either assumes values of μ_a and μ'_s , or derives these values from other measurements. Furthermore, in DCS, the photon DTOF inside the medium

is lost. Therefore, the measured dynamics are obtained from detected signal integrated over all photon path lengths. In order to concurrently measure optical and dynamical properties, DCS and FD NIRS can be combined into one instrument [25, 26]. However, this approach is limited by the need for multiple instruments with different source-detector paths, as well as the inability of DCS to provide time-of-flight resolved measurements.

To solve these problems, we have developed a novel, interferometric near-infrared spectroscopy (iNIRS) method, which simultaneously extracts the optical properties and time-of-flight (TOF) resolved dynamics in turbid media from analysis of the spectral interference fringe pattern. iNIRS measures the spectral interference pattern by using a Mach-Zehnder interferometer (MZI) with a frequency-swept narrow linewidth light source. Since frequency and time are conjugate variables, the time-of-flight difference between light propagating in both interferometer arms can be resolved by Fourier-transforming the spectral or frequency-resolved interference signal. Thus, intensity of light reemitted from the sample can be determined as a function of photon time-of-flight. Therefore, in contrast to DCS, iNIRS can measure intensity fluctuations as a function of time-of-flight. Such an approach has several advantages over typical NIRS/DCS techniques. Notably, iNIRS preserves the DTOF, potentially provides shot-noise limited sensitivity, and most importantly, concurrently determines optical properties and dynamics of the turbid medium using a single optical path. Moreover, analysis of the temporal intensity autocorrelation for a given photon time-of-flight greatly simplifies quantification of scatterer dynamics compared with DCS.

The simultaneous measurement of the photon DTOF and TOF-resolved intensity autocorrelation functions of diffuse light were initiated by Yodh *et al.* [18], who developed pulsed diffusing-wave spectroscopy, in which the TOF-resolved autocorrelation function is measured using nonlinear optical gating. In this approach, however, the path length difference between a reference and sample arm is controlled by an optical delay line. Shifting the reference path repeatedly by tens of centimeters over a few microseconds is challenging. This problem can be solved by employing interferometry, as opposed to nonlinear gating, combined with a frequency-modulated, narrow bandwidth light source [27–30]. In particular, Tualle *et al.* developed an optical setup with a laser swept at a frequency of 10 Hz [27], which was later improved to sweep rates of up to 300 Hz [28]. Recently, another method called frequency-modulated light scattering interferometry was introduced [29, 30]. This technique operates at a rate of 800 Hz. Since multiply scattered light from many samples decorrelates over this time scale, a fitting procedure was used to determine dynamics as well as optical properties from a one-dimensional measurement. By operating more than two orders of magnitude faster than previous techniques, where one laser sweep ($\sim 10 \mu\text{s}$) is smaller than the characteristic decorrelation time, even after multiple scattering events, the method we present here can acquire a two-dimensional (DTOF and autocorrelation decay time) measurement set to determine scatterers' dynamics and optical properties independently. Thus, our method is not limited to static samples and paves the way for real-time determination of the optical properties and blood flow in tissue *in vivo*.

Optical coherence tomography (OCT) [31–34] uses low-coherence interferometry [35, 36] to noninvasively produce cross-sectional images of biological systems with a resolution of a few micrometers and imaging range of several millimeters. Low-coherence interferometry, in this regime, either in the time- or Fourier-domain (swept source or spectral domain), was also used for imaging objects embedded in scattering media using ballistic photons [37, 38], analyzing backscattering as a function of path length using diffusion theory [39], quantifying path length-resolved dynamic properties of diffusive particles [40, 41], and determining optical properties [42, 43]. However, there are major differences between swept source OCT and iNIRS. The goal of iNIRS is to measure optical and dynamical properties of turbid media.

Therefore, iNIRS uses a laser with an instantaneous linewidth and tuning range narrower by several orders of magnitude than in typical OCT systems. This enables measuring distinctly longer photon path lengths (of up to tens of centimeters) at the cost of reduced resolution (of the order of millimeters). Though the light source used here for iNIRS is not suitable for OCT applications, it is appropriate for measuring the photon DTOF in highly scattering media, probing path lengths orders of magnitude higher than what can be assessed using OCT. In other words, iNIRS takes an advantage of multiply scattered photons, which are usually rejected, and most importantly unwanted, in low-coherence interferometry. Moreover, the expression for the instrument response function, governing the capability of iNIRS to resolve the DTOF, departs from the conventional expression for OCT axial resolution. Finally, iNIRS, as implemented here with a single source and detector, is not an imaging or tomography method.

In this paper we lay the theoretical framework for iNIRS and implement it experimentally, simultaneously measuring the photon distribution of time-of-flight and TOF-resolved autocorrelations in turbid media. This enables quantitative determination of both optical properties and scatterer dynamics. We prove this by analyzing the DTOFs of diffusive fluid phantoms with optical thicknesses, defined as geometrical thickness multiplied by μ'_s , of up to 55 transport mean free paths. The optical properties of the phantoms are subsequently determined from the measured DTOFs using the diffusion equation, while dynamic properties of the scatterers are extracted from path length-resolved intensity fluctuations using DWS theory.

Due to relatively large number of symbols and equations, associated with experimental measurements, the diffusion equation (DE), and DWS theory, we use the following naming conventions. Quantities related to a particular theory or technique are marked by an appropriate superscript (DE, DWS, iNIRS), e.g. the scattered light intensity measured using the iNIRS system is denoted as $I_s^{(\text{iNIRS})}$. The (possibly) biased estimates of the experimental quantities are marked by a hat sign. For example $\hat{I}_s^{(\text{iNIRS})}$ denotes the estimated value of $I_s^{(\text{iNIRS})}$ (section 4). The noise-bias-corrected experimental estimates are denoted using tilde, i.e., the symbol $\tilde{I}_s^{(\text{iNIRS})}$ stands for the value of the noise-bias-corrected version of $\hat{I}_s^{(\text{iNIRS})}$.

2. Theory and system design considerations

In this section we present the principles and limitations of iNIRS. We first examine the relationship between the spectral interference pattern, DTOF and TOF-resolved fluctuations of a turbid medium (secs. 2.1 and 2.2). Afterwards, we describe a procedure for extracting the optical and dynamical properties of a turbid medium (sec. 2.3) from measurement of the spectral interference fringe pattern (secs. 2.4 and 2.5).

2.1. Relationship between the optical field and the distribution of photon time-of-flight

The statistical properties of the optical field are characterized by second-order optical coherence theory [44–46]. In this framework, the wide-sense stationary and ergodic optical field at position \mathbf{r} and time t_s can be represented as an analytic signal $U(\mathbf{r}, t_s)$, which can be written as the Fourier integral over optical frequencies, ν :

$$U(\mathbf{r}, t_s) = \int_{-\infty}^{\infty} \mathcal{U}(\mathbf{r}, \nu) \exp[-2\pi i \nu t_s] d\nu. \quad (1)$$

In order to express the iNIRS signal in terms of the optical field, let us associate the functions $U_r(\mathbf{r}, t_s)$ and $U_s(\mathbf{r}, t_s)$ with the reference and sample beams of the MZI, respectively. Then, the iNIRS signal, which is the spectral fringe pattern registered at the exit of the MZI is given by spectral interference law [45, 46] as:

$$\mathcal{S}(\mathbf{r}, \nu) = \mathcal{S}_r(\mathbf{r}, \nu) + \mathcal{S}_s(\mathbf{r}, \nu) + 2\text{Re}[\mathcal{W}_{rs}(\mathbf{r}, \nu)], \quad (2)$$

where

$$\mathcal{W}_{ij}(\mathbf{r}, \mathbf{v}) \delta(\mathbf{v} - \mathbf{v}') = \langle \mathcal{U}_i^*(\mathbf{r}, \mathbf{v}) \mathcal{U}_j(\mathbf{r}, \mathbf{v}') \rangle \quad (3)$$

denotes the cross-spectral density function (power spectrum) of the light field at position \mathbf{r} and optical frequency \mathbf{v} . Furthermore $\mathcal{S}_i(\mathbf{r}, \mathbf{v}) = \mathcal{W}_{ii}(\mathbf{r}, \mathbf{v})$ denotes the spectral density of the optical field $U_i(\mathbf{r}, t_s)$ and $\langle \dots \rangle$ stands for ensemble averaging.

According to the Wiener-Khintchine theorem [45, 47, 48], the cross-spectral density function $\mathcal{W}_{ij}(\mathbf{r}, \mathbf{v})$ is a Fourier transform

$$\mathcal{W}_{ij}(\mathbf{r}, \mathbf{v}) = \int_{-\infty}^{\infty} \Gamma_{ij}(\mathbf{r}, \tau_s) \exp[2\pi i \mathbf{v} \tau_s] d\tau_s \quad (4)$$

of the mutual coherence (field autocorrelation) function

$$\Gamma_{ij}(\mathbf{r}, \tau_s) = \langle U_i^*(\mathbf{r}, t_s) U_j(\mathbf{r}, t_s + \tau_s) \rangle_{t_s} = \lim_{T \rightarrow \infty} \frac{1}{2T} \int_{-T}^T U_i^*(\mathbf{r}, t_s) U_j(\mathbf{r}, t_s + \tau_s) dt_s, \quad (5)$$

where τ_s denotes the delay time between the two arms of the MZI. On the grounds of Eq. (4) and Eq. (5) the spectral fringe pattern $\mathcal{S}(\mathbf{r}, \mathbf{v})$ can be converted to an autocorrelation by using an inverse Fourier transformation. This procedure yields:

$$I(\mathbf{r}, \tau_s) = \Gamma_r(\mathbf{r}) + \Gamma_s(\mathbf{r}) + \Gamma_{rs}(\mathbf{r}, \tau_s) + \Gamma_{sr}(\mathbf{r}, \tau_s), \quad (6)$$

where $\Gamma_i(\mathbf{r}) = \Gamma_{ii}(\mathbf{r}, 0)$. The first two terms on the right-hand side of Eq. (6) constitute the DC term $\Gamma_{DC}(\mathbf{r}) = \Gamma_r(\mathbf{r}) + \Gamma_s(\mathbf{r})$, which does not carry useful information about the photon DTOF. $\Gamma_r(\mathbf{r})$ is the light intensity from the reference arm of the interferometer, while $\Gamma_s(\mathbf{r})$ is the light intensity from the sample arm. The value of $\Gamma_r(\mathbf{r})$ can be determined in a separate measurement (when the sample arm is blocked) and subsequently subtracted from Eq. (6). Similarly, the value of $\Gamma_s(\mathbf{r})$ can be determined by blocking the interferometer reference arm, though it is small for most diffuse samples. Alternatively, a dual-balanced detector may be used to eliminate $\Gamma_{DC}(\mathbf{r})$. This leaves the sum of cross-terms, i.e. $\Gamma_{rs}(\mathbf{r}, \tau_s) + \Gamma_{sr}(\mathbf{r}, \tau_s)$. Both of these terms represent the correlation function between the reference optical field $U_r(\mathbf{r}, t_s)$ of the light which travels a fixed distance, and the optical field $U_s(\mathbf{r}, t_s)$ of the light which emerges from the turbid medium. Therefore, the cross-terms can be used to determine the amplitude and phase of $U_s(\mathbf{r}, t_s)$ and in turn to recover information about the photon time-of-flight distribution or, in other words, intensity as a function of τ_s . This time-resolved photon distribution (DTOF), can be converted into a path length-resolved photon distribution by taking into account the speed of light in the medium.

However, according to Eq. (2), only the real part of the cross-spectral density is measured. The corresponding sum of cross-terms is Hermitian, since $\Gamma_{rs}(\mathbf{r}, \tau_s) = \Gamma_{sr}^*(\mathbf{r}, -\tau_s)$, which shows that the cross-terms constitute a pair of mirrored components. Thus, unique information about the DTOF is limited to either positive or negative values of τ_s . The effect of mirror terms reduces the usable TOF range by a factor of two. Nonetheless, the TOF range can be recovered by reconstructing the phase of the cross-spectral density function such that its Fourier transformation does not contain overlapping mirror terms [49].

We shall now calculate $\Gamma_{rs}^{(iNIRS)}(\mathbf{r}, \tau_s)$ measured using the iNIRS system at time t_d , included henceforth as a third argument to all functions defined in Eqs. (1)–(6). For this purpose we assume that the optical components of the reference arm of the interferometer introduce a constant relative attenuation, α_r , a random time- and position-dependent phase shift, $\varphi_r(\mathbf{r}, t_d)$, and a delay, τ_r , of the optical field at the interferometer entrance, denoted by $U_{inc}(t_s)$. The time-dependence of the phase shift $\varphi_r(\mathbf{r}, t_d)$ accounts for possible interferometer drift. Let us further assume that the optical field of the light emerging from the turbid medium is composed of N

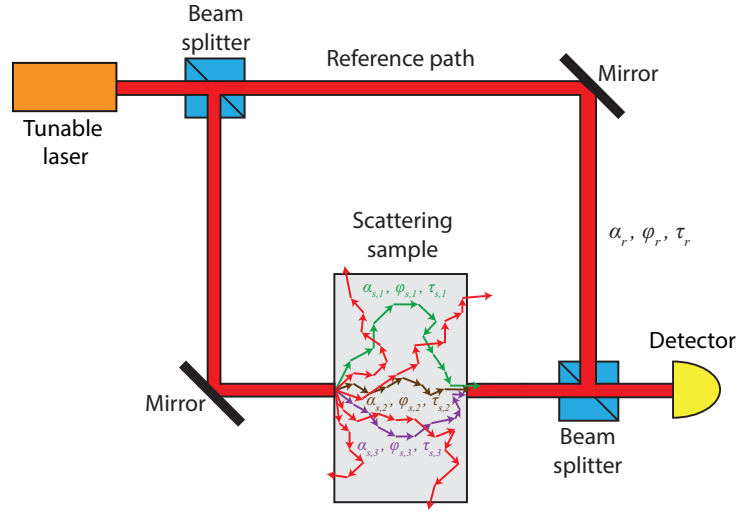


Fig. 1. Geometry for the calculation of the autocorrelation function $\Gamma_{rs}^{(iNIRS)}$ of the reference and multiply scattered sample light fields. The real part of the cross-spectral density function is measured by a detector at the exit of the Mach-Zehnder interferometer and used to determine the autocorrelation function [see Eq. (4)].

uncorrelated photon paths, each of length $l_n = v\tau_{s,n}$, where $n = 1, \dots, N$ and v denotes the speed of light in the medium. Though not explicitly a function of \mathbf{r} , the photon paths depend on the detector position, in general. The optical field associated with each photon path can be described by the relative light attenuation $\alpha_{s,n}(\mathbf{r})$, phase shift $\varphi_{s,n}(\mathbf{r}, t_d)$ and delay of $\tau_{s,n}$ [Fig. 1]. Under these assumptions the reference and sample fields, i.e. $U_r(\mathbf{r}, t_s, t_d)$ and $U_s(\mathbf{r}, t_s, t_d)$, can be written as

$$U_r(\mathbf{r}, t_s, t_d) = \alpha_r \exp[i\varphi_r(\mathbf{r}, t_d)] U_{\text{inc}}(t_s - \tau_r), \quad (7)$$

$$U_s(\mathbf{r}, t_s, t_d) = \sum_{n=1}^N \alpha_{s,n}(\mathbf{r}) \exp[i\varphi_{s,n}(\mathbf{r}, t_d)] U_{\text{inc}}(t_s - \tau_{s,n}). \quad (8)$$

Photon paths that do not contribute to the sample field at the detector are assigned a corresponding $\alpha_{s,n}(\mathbf{r})$ value of zero. After substituting Eq. (7) and Eq. (8) into definition (5), with the understanding that averaging is performed over the measurement time, one obtains:

$$\Gamma_{rs}^{(iNIRS)}(\mathbf{r}, \tau_s, t_d) = \alpha_r \sum_{n=1}^N \alpha_{s,n}(\mathbf{r}) \exp[-i\Delta\varphi_{rs,n}(\mathbf{r}, t_d)] \Gamma_{\text{inc}}(\tau_s - \tau'_{s,n}), \quad (9)$$

where

$$\Delta\varphi_{rs,n}(\mathbf{r}, t_d) = \varphi_r(\mathbf{r}, t_d) - \varphi_{s,n}(\mathbf{r}, t_d)$$

and

$$\Gamma_{\text{inc}}(\tau_s) = \langle U_{\text{inc}}^*(t_s) U_{\text{inc}}(t_s + \tau_s) \rangle_{t_s}, \quad (10)$$

stands for the mutual coherence function of the incident optical field, and $\tau'_{s,n} = \tau_{s,n} - \tau_r$. Note that although the $\tau'_{s,n}$ that contribute to the summation in Eq. (9) depend on detector position, the explicit \mathbf{r} dependence has been incorporated into $\alpha_{s,n}(\mathbf{r})$. We have assumed that attenuations α_r and $\alpha_{s,n}(\mathbf{r})$ are time-independent. Provided that the time-scale of fluctuations of the phase component [23], $\exp[-i\Delta\varphi_{rs,n}(\mathbf{r}, t_d)]$, is larger than the measurement time, this term can be brought outside the averaging brackets in Eq. (9).

Expression (9) shows that for fixed t_d , $\Gamma_{rs}^{(\text{iNIRS})}(\mathbf{r}, \tau_s, t_d)$ is a weighted sum of the contributions from each photon path length. Moreover, $\Gamma_{rs}^{(\text{iNIRS})}(\mathbf{r}, \tau_s, t_d)$ is a complex function, proportional to the sample field. However, random phases lead to the interference of scattered wavefronts, which in turn, generates a speckle pattern [50–52]. To overcome the destructive effect of speckles, the photon TOF distribution is obtained by temporal averaging:

$$I_s^{(\text{iNIRS})}(\mathbf{r}, \tau_s) = \left\langle \left| \Gamma_{rs}^{(\text{iNIRS})}(\mathbf{r}, \tau_s, t_d) \right|^2 \right\rangle_{t_d}, \quad (11)$$

where the subscript t_d indicates averaging over consecutive measurements. To achieve speckle reduction, the time window for averaging must be much larger than the speckle correlation time. In order to evaluate this average one substitutes expression (9) into Eq. (11) and obtains:

$$I_s^{(\text{iNIRS})}(\mathbf{r}, \tau_s) = \alpha_r^2 \sum_{n=1}^N \sum_{m=1}^N \alpha_{s,n}(\mathbf{r}) \alpha_{s,m}(\mathbf{r}) \Gamma_{\text{inc}}^*(\tau_s - \tau'_{s,n}) \Gamma_{\text{inc}}(\tau_s - \tau'_{s,m}) \times \langle \exp \{ i [\Delta\phi_{rs,n}(\mathbf{r}, t_d) - \Delta\phi_{rs,m}(\mathbf{r}, t_d)] \} \rangle_{t_d}. \quad (12)$$

Phase components $\exp[i\Delta\phi_{rs,n}(\mathbf{r}, t_d)]$ are assumed to be random processes of zero mean. Furthermore, phase components corresponding to different photon paths are assumed to be statistically uncorrelated [53]. Hence, the time-averages of phase components yield non-zero contributions to the double summation on the right-hand side of Eq. (12) for $n = m$ only. Therefore, expression (11) reduces to

$$I_s^{(\text{iNIRS})}(\mathbf{r}, \tau_s) = \sum_{n=1}^N I_{s,n}(\mathbf{r}) \left| \Gamma_{\text{inc}}(\tau_s - \tau'_{s,n}) \right|^2, \quad (13)$$

where $I_{s,n}(\mathbf{r}) = \alpha_r^2 \alpha_{s,n}^2(\mathbf{r})$ is proportional to the intensity for the n -th photon path.

If the N photon paths can be treated as a continuous integral over τ_s , expression (13) can be generalized to the following form:

$$I_s^{(\text{iNIRS})}(\mathbf{r}, \tau_s) = \int_{-\infty}^{\infty} d\tau'_s I_s(\mathbf{r}, \tau'_s) I_0(\tau_s - \tau'_s), \quad (14)$$

where

$$I_0(\tau_s) = \left| \Gamma_{\text{inc}}(\tau_s) \right|^2 \quad (15)$$

stands for the instrument response function (IRF). In practice, the instrument response function may be delayed (i.e. shifted in τ_s) to achieve correspondence between I_s and DTOFs predicted by diffusion theory. The particular issue of time reference is discussed further under section 4.

Equation (14) shows that photon DTOF measured using iNIRS is convolved with the IRF, which depends on the mutual coherence function of the incident optical field, $\Gamma_{\text{inc}}(\tau_s)$. From the definition in Eq. (4), $\Gamma_{\text{inc}}(\tau_s)$ is the inverse Fourier transform of the light source spectrum:

$$\Gamma_{\text{inc}}(\tau_s) = \mathcal{F}^{-1} \{ \mathcal{S}_{\text{inc}}(\mathbf{v}) \}, \quad (16)$$

where \mathcal{F} is the Fourier operator. As a consequence, $\Gamma_{\text{inc}}(\tau_s)$ depends on the spectral properties of the light source. For the idealized case of the light source with an infinite-width spectrum, $\Gamma_{\text{inc}}(\tau_s) = \delta(\tau_s)$. Hence, the resulting intensity distribution $I_s^{(\text{iNIRS})}(\mathbf{r}, \tau_s)$ would accurately describe the DTOF. On the other hand, for a finite-width spectrum of the incident optical field, $\Gamma_{\text{inc}}(\tau_s)$, is not a delta function. Therefore, the distribution of $I_s^{(\text{iNIRS})}(\mathbf{r}, \tau_s)$ is blurred. This effect is sketched in Fig. 2.

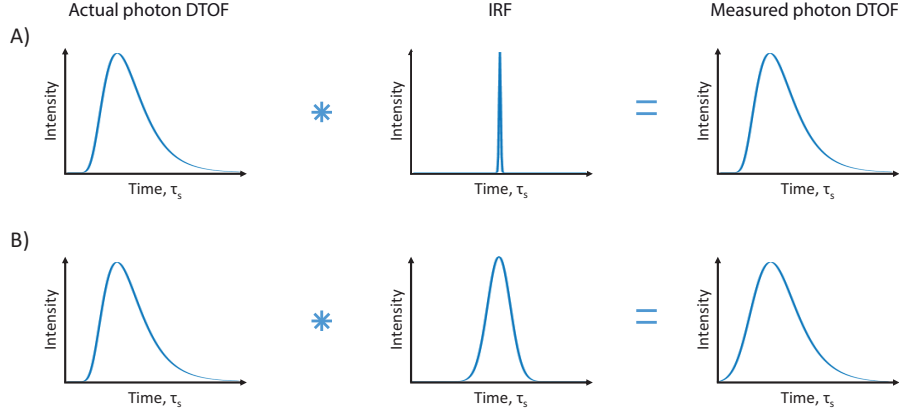


Fig. 2. Dependence of measured photon TOF distribution on the instrument response function (IRF), proportional to the modulus-squared of the mutual coherence function (field autocorrelation) of the incident optical field, $\Gamma_{\text{inc}}(\tau_s)$. (A) For a very narrow mutual coherence function (infinite-width spectrum of incident light), the measured TOF distribution $I_s^{(\text{iNIRS})}(\mathbf{r}, \tau_s)$ precisely reflects the actual photon DTOF $I_s(\mathbf{r}, \tau_s)$. (B) The measured photon DTOF is blurred when the mutual coherence function of the incident optical field is not a delta function (finite-width spectrum of incident light).

2.2. Optical field fluctuations and the dynamic properties of the turbid medium

Light propagating in a turbid medium is scattered from dynamic particles that impart frequency shifts to the detected light. This leads to fluctuations and hence, decorrelation of the complex optical field over time, a phenomenon which forms the basis of dynamic light scattering-based methods. Thus, by analyzing the fluctuations of the sample field $\Gamma_{rs}^{(\text{iNIRS})}(\mathbf{r}, \tau_s, t_d)$, one can determine the dynamic properties of scatterers. This requires knowledge of the first-order normalized optical field autocorrelation function:

$$g_1^{(\text{iNIRS})}(\mathbf{r}, \tau_s, \tau_d) = \frac{G_1^{(\text{iNIRS})}(\mathbf{r}, \tau_s, \tau_d)}{G_1^{(\text{iNIRS})}(\mathbf{r}, \tau_s, 0)}, \quad (17)$$

where

$$G_1^{(\text{iNIRS})}(\mathbf{r}, \tau_s, \tau_d) = \left\langle \Gamma_{rs}^{*(\text{iNIRS})}(\mathbf{r}, \tau_s, t_d) \Gamma_{rs}^{(\text{iNIRS})}(\mathbf{r}, \tau_s, t_d + \tau_d) \right\rangle_{t_d}. \quad (18)$$

The autocorrelation function defined in Eq. (17) depends on the two time parameters: τ_d and τ_s . Here, τ_d has to be explicitly distinguished from τ_s , since the time scale of the former is related to dynamics or motion, while the latter refers to the delay between the two interferometer arms or photon time-of-flight.

The function $g_1^{(\text{iNIRS})}(\mathbf{r}, \tau_s, \tau_d)$ quantifies the temporal autocorrelation between the optical fields scattered by the sample at time lag τ_d and the time-of-flight τ_s . This function is distinguished from $\Gamma_{rs}^{(\text{iNIRS})}(\mathbf{r}, \tau_s, t_d)$, which is the autocorrelation of the reference and sample fields. In our experiments, $\Gamma_{rs}^{(\text{iNIRS})}(\mathbf{r}, \tau_s, t_d)$ is determined by Fourier analysis of the spectral interference fringe pattern, while the information about the motion of scatterers is determined digitally by estimating $g_1^{(\text{iNIRS})}(\mathbf{r}, \tau_s, \tau_d)$. Thus, we require that the measurement time is much smaller than the time scale of decorrelation caused by sample dynamics. Provided that this condition holds, iNIRS is able to take a "snapshot" of the sample field.

By substituting expression (9) into definition (18) and performing the same steps as used in derivation of Eq. (13) one obtains

$$G_1^{(\text{iNIRS})}(\mathbf{r}, \tau_s, \tau_d) = \alpha_r^2 \sum_{n=1}^N \alpha_{s,n}^2(\mathbf{r}) \langle \exp[i\Delta\Phi_{rs,n}(\mathbf{r}, t_d, \tau_d)] \rangle_{t_d} |\Gamma_{\text{inc}}(\tau_s - \tau'_{s,n})|^2, \quad (19)$$

where

$$\Delta\Phi_{rs,n}(\mathbf{r}, t_d, \tau_d) = \Delta\phi_{rs,n}(\mathbf{r}, t_d) - \Delta\phi_{rs,n}(\mathbf{r}, t_d + \tau_d).$$

By noting that

$$G_{1,n}(\mathbf{r}, \tau_d) = I_{s,n}(\mathbf{r}) \langle \exp[i\Delta\Phi_{rs,n}(\mathbf{r}, t_d, \tau_d)] \rangle_{t_d}$$

is known from DWS as the first-order field autocorrelation function of the n -th photon path, expression (19) can be rewritten as

$$G_1^{(\text{iNIRS})}(\mathbf{r}, \tau_s, \tau_d) = \sum_{n=1}^N G_{1,n}(\mathbf{r}, \tau_d) |\Gamma_{\text{inc}}(\tau_s - \tau'_{s,n})|^2. \quad (20)$$

The above result shows that the sample field, $\Gamma_{rs}^{(\text{iNIRS})}(\mathbf{r}, \tau_s, t_d)$ will decorrelate over time at a rate dependent on the phase decorrelation along individual paths.

The right hand side of Eq. (20) can be now generalized to a continuous integral over τ_s [similar to Eq. (14)]:

$$G_1^{(\text{iNIRS})}(\mathbf{r}, \tau_s, \tau_d) = \int_{-\infty}^{\infty} d\tau'_s G_1(\mathbf{r}, \tau'_s, \tau_d) I_0(\tau_s - \tau'_s). \quad (21)$$

Equation (21) relates the conventional field autocorrelation function to the one measured using the iNIRS method. Since Eq. (21) is a convolution, iNIRS enables windowing of the TOF-resolved autocorrelation function $G_1(\mathbf{r}, \tau_s, \tau_d)$ with the instrument response function (IRF). In particular, for $\Gamma_{\text{inc}}(\tau_s) = \delta(\tau_s)$, relation (21) reduces precisely to the results derived in [13, 18]. Therefore, $G_1^{(\text{iNIRS})}(\mathbf{r}, \tau_s, \tau_d)$, can be used to extract TOF-resolved dynamic properties of highly scattering samples.

To relate the scattered field autocorrelation function to measured DTOF $I_s^{(\text{iNIRS})}(\mathbf{r}, \tau_s)$ it is sufficient to evaluate $G_1^{(\text{iNIRS})}(\mathbf{r}, \tau_s, \tau_d)$ at $\tau_d = 0$. In this case, Eq. (21) reduces to expression (14).

The direct calculation of the function $g_1^{(\text{iNIRS})}(\mathbf{r}, \tau_s, \tau_d)$ from measurements of $\Gamma_{rs}^{(\text{iNIRS})}(\mathbf{r}, \tau_s, t_d)$ may be sensitive to phase instabilities in the iNIRS system [cf. Eq. (19)]. Therefore, in order to determine $g_1^{(\text{iNIRS})}(\mathbf{r}, \tau_s, \tau_d)$ we use the normalized intensity autocorrelation function (the second-order field autocorrelation),

$$g_2^{(\text{iNIRS})}(\mathbf{r}, \tau_s, \tau_d) = \frac{G_2^{(\text{iNIRS})}(\mathbf{r}, \tau_s, \tau_d)}{[G_1^{(\text{iNIRS})}(\mathbf{r}, \tau_s, 0)]^2}, \quad (22)$$

with

$$G_2^{(\text{iNIRS})}(\mathbf{r}, \tau_s, \tau_d) = \left\langle \left| \Gamma_{rs}^{(\text{iNIRS})}(\mathbf{r}, \tau_s, t_d) \right|^2 \left| \Gamma_{rs}^{(\text{iNIRS})}(\mathbf{r}, \tau_s, t_d + \tau_d) \right|^2 \right\rangle_{t_d}.$$

Then, as in typical DCS experiments, the first-order field autocorrelation function can be extracted from the intensity autocorrelation by using the Siegert relation [20]:

$$g_2^{(\text{iNIRS})}(\mathbf{r}, \tau_s, \tau_d) = 1 + \beta \left| g_1^{(\text{iNIRS})}(\mathbf{r}, \tau_s, \tau_d) \right|^2, \quad (23)$$

where the parameter $\beta \in (0, 1]$ accounts for the number of measured speckles [23]. According to definition (17), $g_1^{(\text{iNIRS})}(\mathbf{r}, \tau_s, \tau_d) \rightarrow 1$ as $\tau_d \rightarrow 0$. Thus, the value of the parameter β can be calculated from the intensity autocorrelation function, $g_2^{(\text{iNIRS})}(\mathbf{r}, \tau_s, \tau_d)$, by using the following expression

$$\beta = g_2^{(\text{iNIRS})}(\mathbf{r}, \tau_s, 0) - 1. \quad (24)$$

Alternatively, the value of β can be determined from the following relation

$$\beta = \frac{G_2^{(\text{iNIRS})}(\mathbf{r}, \tau_s, 0) - G_2^{(\text{iNIRS})}(\mathbf{r}, \tau_s, \infty)}{G_2^{(\text{iNIRS})}(\mathbf{r}, \tau_s, \infty)}, \quad (25)$$

since $g_1^{(\text{iNIRS})}(\mathbf{r}, \tau_s, \tau_d) \rightarrow 0$ for $\tau_d \rightarrow \infty$.

In summary, information about sample dynamics can be distinguished from optical properties (μ_a, μ'_s) when the following two conditions are met. The first condition is that the characteristic field autocorrelation decay time τ_d is much greater than measurement time. The second condition, discussed in greater detail below, is that the light source coherence time is larger than the required photon time-of-flight range.

2.3. Relation between optical and dynamical properties and the diffuse optical field autocorrelation

The optical properties of a turbid medium can be extracted from experimentally measured values of the function $I_s^{(\text{iNIRS})}(\mathbf{r}, \tau_s)$ using the diffusion approximation to the radiative transfer equation (RTE) for the fluence rate [54, 55]. In particular, for a narrow collimated pulse of light normally incident (propagation along the z -axis) on a homogeneous slab of thickness L and by imposing the extrapolated boundary condition, in which the fluence rate is equal to zero at each extrapolated boundary, one obtains [7, 56, 57]:

$$I_s^{(\text{DE})}(\rho, L, \tau_s) = \frac{\exp[-\mu_a \nu \tau_s]}{2\pi\sigma_t^2 \tau_s \sqrt{4D\nu\tau_s}} \exp\left[-\frac{\rho^2}{2\sigma_t^2}\right] \sum_{m=-\infty}^{\infty} \left\{ (L - z_{+,m}) \exp\left[-\frac{(L - z_{+,m})^2}{4D\nu\tau_s}\right] - (L - z_{-,m}) \exp\left[-\frac{(L - z_{-,m})^2}{4D\nu\tau_s}\right] \right\}, \quad (26)$$

where ν is the speed of light in the slab, ρ denotes the Euclidean distance from the z -axis (source-detector separation), $D = \frac{1}{3\mu'_s}$ stands for the diffusion coefficient, and $\sigma_t^2 = \sigma_s^2 + \sigma_d^2 + 2D\nu\tau_s$. The finite detector size as well as the extended light source were incorporated by convolving the original solution given in [7, 56, 57] with two Gaussian functions, describing the collimated modes from the source and detector fibers. These functions are assumed to have a standard deviations of σ_d and σ_s , respectively. Furthermore,

$$z_{+,m} = 2m(L + 2z_e) + z_0,$$

$$z_{-,m} = 2m(L + 2z_e) - 2z_e - z_0$$

denote the locations of the isotropic point sources [Fig. 3] required to satisfy extrapolated boundary conditions. In the above equations $z_0 = 1/\mu'_s$ denotes the depth at which all of the incident photons are diffuse and $z_e = 2AD$ is the location of the extrapolated boundary. The coefficient A is defined as

$$A = \frac{1 + R(n)}{1 - R(n)},$$

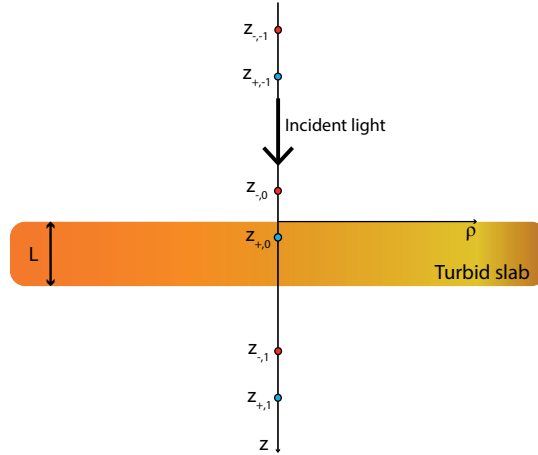


Fig. 3. Geometry for the calculation of the time-resolved transmittance through a homogeneous turbid slab (after [7, 57]). The locations of the first positive (blue dots) and negative (red dots) isotropic point sources are shown.

where $R(n)$ denotes the reflection coefficient [57]:

$$R(n) = -1.4399n^{-2} + 0.7099n^{-1} + 0.6681 + 0.0636n,$$

which depends on the refractive index mismatch n between the diffusive medium and its surroundings. The solution given in Eq. (26) does not depend on θ due to cylindrical symmetry.

Equation (26) represents the probability per unit time of detecting photons emerging from a diffusive homogeneous slab at time τ_s at the detector located a distance ρ from the z -axis. The function $I_s^{(DE)}(\rho, L, \tau_s)$ therefore represents the photon distribution of time-of-flight, measured in transmission geometry. The infinite summation in Eq. (26) is over the virtual isotropic point sources shown in Fig. 3. In this work we truncated this series at $m = \pm 20$.

On the other hand, the dynamic properties of the scatterers can be extracted from the first-order field autocorrelation function $G_1^{(iNIRS)}(\mathbf{r}, \tau_s, \tau_d)$ using DWS theory [14, 58] or the diffusion correlation equation [17, 22–24]. In the DWS framework, the normalized TOF-resolved first-order field autocorrelation function of a suspension of identical noninteracting particles with a Brownian diffusion coefficient D_B does not depend on \mathbf{r} and is given by

$$g_1^{(DWS)}(\tau_s, \tau_d) = \exp \left[-\frac{1}{3} k^2 \mu'_s \langle \Delta r^2(\tau_d) \rangle \nu \tau_s \right], \quad (27)$$

where k is the wave number of light in the sample. Furthermore, $\langle \Delta r^2(\tau_d) \rangle$ is the time-dependent mean-square displacement of the scatterers. In particular, for Brownian diffusion $\langle \Delta r^2(\tau_d) \rangle = 6D_B \tau_d$. It follows therefore that the autocorrelation function decays exponentially and the decay rate, $\xi = 2k^2 D_B \mu'_s \nu \tau_s$ is proportional to the product of D_B , μ'_s , and photon path length $\nu \tau_s$.

DCS measurement techniques are unable to determine dynamic properties independently of optical properties for two reasons. First, a weighted average of Eq. (27) over the photon time-of-flight distribution, which depends on medium optical properties, must be performed in DCS to account for the lack of TOF resolution. Second, the decay rate of the TOF-resolved autocorrelation in Eq. (27) depends on μ'_s . iNIRS addresses the first issue directly by enabling TOF resolution, and addresses the second issue indirectly by quantifying scattering independently through DTOF analysis.

Lastly, we note that, though it was not explicitly utilized here, DCE theory [17, 21–24] provides unnormalized autocorrelation functions (equivalent to normalized autocorrelation functions and intensity DTOFs) in a single framework.

2.4. Measurement of spectral interference pattern

Though not treated above in the theory section, a number of practical experimental issues arise in measuring the spectral interference pattern. In iNIRS the spectral interference fringe pattern is measured using a rapidly tunable laser, though other approaches such as high-resolution spectrometers are possible [41, 59]. For iNIRS, as shown in Fig. 4, one may visualize the spectral interference pattern as being generated in the time domain from the beating of the frequency sweep and a copy of the frequency sweep, delayed in time.

For this series of experiments, the wavelength of a short-cavity distributed feedback laser is swept in time by modulating the drive current. However, *in vivo* applications require fast tuning repetition rates or sweep rates, $f_t = 2f_r$, where $f_r = 1/t_m$ is the laser modulation frequency and t_m is the measurement time interval. As tuning frequency increases, the dominant mechanism of laser wavelength tuning switches from thermal to carrier density modulation. This leads to a reduction in the tuning parameter (given in GHz/mA), which in turn degrades the tuning range, $\Delta\nu$ [60]. As a consequence the time resolution, $\delta\tau_s$, becomes worse, as will be shown in section 2.5. An increasing laser tuning speed (given in GHz/s) diminishes the detection sensitivity due to a lower number of detected photons per sweep [34] and also broadens the instantaneous laser spectral linewidth, $\delta\nu$ [61]. Although the sensitivity can be recovered by increasing the number of consecutive measurements and averaging, the linewidth broadening irreversibly decreases the time-of-flight measurement range or coherence time, τ_c . Dependence of the time resolution and measurement range on the parameters of the light source are further discussed in section 2.5.

For the above reasons, the laser sweep rate cannot be arbitrarily increased. For our experiments, we chose a laser sweep rate of 100 kHz, leading to a sweep time or measurement time $t_m/2$ of approximately 10 microseconds. Due to the assumption that decorrelation over the sweep is negligible, the current iNIRS technique can be applied to samples for which the intrinsic decorrelation time is greater than ten microseconds, which is a typical value in biological tissue for source-detector separations not larger than 2 cm [23], although decorrelation time depends on time-of-flight in general. Due to the complex tuning mechanisms and limited tuning bandwidth, such fast sweep rates were achieved with a sinusoidal (nonlinear) modulation. As shown in Fig. 4(c), nonlinear tuning of the laser wavelength leads to a non-uniform beat frequency. However, a Fourier transform relationship assumes that a single beat frequency corresponds to a single time-of-flight. Thus, if not compensated, the non-uniform beat frequency invalidates the Fourier analysis used in iNIRS. For this study, the nonlinear sweep was compensated by means of a recalibration procedure before applying Fourier transformation to the detected signal, as described in section 4.

2.5. Resolution and measurement range

Let us now briefly discuss the impact of light source tuning parameters on the TOF resolution of the iNIRS system. One may distinguish two measurement stages in iNIRS. The first is a time series of measurements of the instantaneous optical field transmission of the sample, denoted by $\Gamma_{rs}^{(iNIRS)}(\mathbf{r}, \tau_s, t_d)$ [cf. Eq. (9)], while the second uses time-averaged (over t_d) values of $\left| \Gamma_{rs}^{(iNIRS)}(\mathbf{r}, \tau_s, t_d) \right|^2$ to obtain the photon DTOF $I_s^{(iNIRS)}(\mathbf{r}, \tau_s)$.

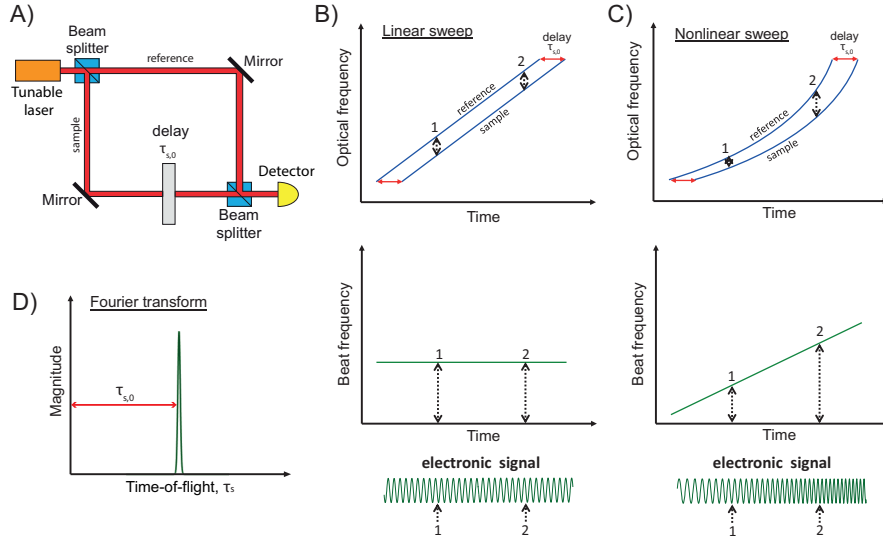


Fig. 4. Measurement of the spectral interference pattern and a simple illustration of a linear versus nonlinear frequency sweep in iNIRS. A) The sample placed in the interferometer sample arm delays the optical field from the frequency-swept light source by a time $\tau_{s,0}$. Practically, this delay must be shorter than the coherence time, which in turn is less than the sweep time of our laser. B) Due to the fact that the laser frequency is changed over time, or "swept", photons which take a longer time to travel through one interferometer arm will generate a larger beat frequency upon interference. Hence for a linear sweep, iNIRS encodes time delay, $\tau_{s,0}$ as beat frequency. C) For a nonlinear sweep, delay is still encoded as beat frequency; however the beat frequency is no longer constant versus time. This nonlinearity in the beat frequency can be accounted for through a numerical recalibration procedure described in section 4. Because time delay is encoded in the beat frequency, the value of $\tau_{s,0}$ can be determined by inverse Fourier-transforming the electronic interference signal (D).

To interpret the physical meaning of $\Gamma_{rs}^{(iNIRS)}(\mathbf{r}, \tau_s, t_d)$ we rewrite Eq. (9) as:

$$\Gamma_{rs}^{(iNIRS)}(\mathbf{r}, \tau_s, t_d) = \Gamma_{rs}(\mathbf{r}, \tau_s, t_d) * \Gamma_{inc}(\tau_s), \quad (28)$$

where

$$\Gamma_{rs}(\mathbf{r}, \tau_s, t_d) = \alpha_r \sum_{n=1}^N \alpha_{s,n}(\mathbf{r}) \exp[-i\Delta\phi_{rs,n}(\mathbf{r}, t_d)] \delta(\tau_s - \tau'_{s,n})$$

and $*$ denotes convolution with respect to τ_s .

According to Eq. (28), the measurement of $\Gamma_{rs}^{(iNIRS)}(\mathbf{r}, \tau_s, t_d)$ is equal to the optical field transmission, convolved with $\Gamma_{inc}(\tau_s)$. Thus, if an infinitely narrow pulse, or delta function, were incident on the sample from the source position, the measured electric field response at the detector would be given by $\Gamma_{rs}(\mathbf{r}, \tau_s, t_d)$. Thus $\Gamma_{rs}(\mathbf{r}, \tau_s, t_d)$ may be considered as the field "impulse response" of the medium describing the cumulative phase shifts, attenuations, and time shifts of the various photon paths. The interpretation of the convolution expression (28) is that the resolution for measuring the field transmission function is determined by the shape of the function $\Gamma_{inc}(\tau_s)$ [cf. Eq. (16)]. In particular, for a Gaussian with a frequency bandwidth of

Δv at the full width at half maximum (FWHM), centered at v_c ,

$$\mathcal{S}_{\text{inc}}(v) = \exp \left[-4 \ln(2) \left(\frac{v - v_c}{\Delta v} \right)^2 \right], \quad (29)$$

which due to the positivity of Δv yields

$$\Gamma_{\text{inc}}(\tau_s) = \frac{\sqrt{\pi} \Delta v}{2\sqrt{\ln(2)}} \exp \left[- \left(\frac{\pi \Delta v \tau_s}{2\sqrt{\ln(2)}} \right)^2 \right] \exp[-2\pi i v_c \tau_s]. \quad (30)$$

The modulus of the above is a Gaussian distribution with a standard deviation of $\sigma = \frac{\sqrt{2 \ln(2)}}{\pi \Delta v}$. The FWHM of such a Gaussian function defines the TOF resolution $\delta \tau_s$ of the measured $\Gamma_{rs}^{(\text{iNIRS})}(\mathbf{r}, \tau_s, t_d)$. By using the well-known relationship between the FWHM of a Gaussian function and its standard deviation σ ,

$$\text{FWHM} = 2\sqrt{2 \ln(2)} \sigma,$$

one obtains an explicit equation for $\delta \tau_s$:

$$\delta \tau_s = \frac{4 \ln(2)}{\pi \Delta v} = \frac{4 \ln(2)}{\pi} \frac{\lambda_c^2}{v \Delta \lambda}, \quad (31)$$

where λ_c is the laser central vacuum wavelength and $\Delta \lambda = \lambda_c^2 \Delta v / v$ is the wavelength bandwidth. Note that $\Gamma_{\text{inc}}(\tau_s)$ is analogous to the commonly used point spread function in OCT [32, 33], excepting the factor of 2 difference in width due to the single-pass geometry in iNIRS.

In general the measured $\Gamma_{rs}^{(\text{iNIRS})}(\mathbf{r}, \tau_s, t_d)$ will be affected by speckle (due to the random phases of paths adding together within a resolution element). To experimentally measure the photon time-of-flight distribution, proportional to time-resolved intensity, the modulus-squared of the field transmission function is averaged over time [see Eq. (11)]. This time-averaged intensity can then be compared to theoretical DTOFs determined from time-resolved diffusion theory [cf. Eq. (26)], to infer bulk optical properties. Taking this time-averaging into account, the time-of-flight resolved intensity measured by iNIRS is given by [cf. Eq. (14)]:

$$I_s^{(\text{iNIRS})}(\mathbf{r}, \tau_s) = I_s(\mathbf{r}, \tau_s) * I_0(\tau_s), \quad (32)$$

The interpretation of this expression is that the resolution for estimating the DTOF is determined by the shape of $I_0 = |\Gamma_{\text{inc}}(\tau_s)|^2$, which determines IRF [cf. Eq. (15)]. If $\Gamma_{\text{inc}}(\tau_s)$ is Gaussian, so is $|\Gamma_{\text{inc}}(\tau_s)|^2$, but it is narrower by a factor of $\sqrt{2}$. Therefore the resolution, $\delta \tau_{s, I_s}$ of DTOF is improved by a factor of $\sqrt{2}$ when measuring the time-averaged intensity [cf. Eq. (32)], as compared with the instantaneous field transmission given in expression (31), i.e.:

$$\delta \tau_{s, I_s} = \frac{\delta \tau_s}{\sqrt{2}}.$$

Another important consideration for frequency tunable or swept lasers in iNIRS is the measurable TOF range. For a stationary (not tuned) laser, the coherence time (or length), inversely proportional to the spectral linewidth, defines the range of time delays (or path delays) that can be measured using interferometry. More precisely, the coherence function, the inverse Fourier transform of the spectrum, defines the fringe visibility (Michelson contrast) as a function of time delay [44–46].

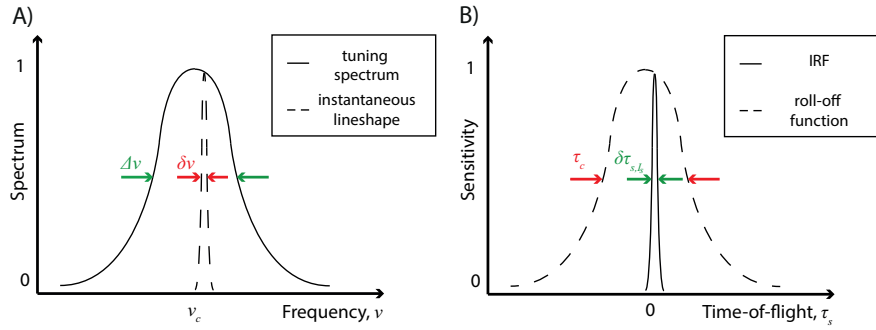


Fig. 5. Dependence of measurement range and resolution on laser tuning parameters. The instantaneous linewidth, $\delta\nu$ (A) is related to the coherence time, τ_c or time-of-flight (TOF) range (B) of the measurement (dashed lines), while the overall bandwidth over which the laser frequency is tuned, $\Delta\nu$ (A), is related to the FWHM of the TOF resolution, $\delta\tau_{s,l}$ (B), of the measurement (solid lines) [33]. The TOF resolution, determined by the tuning spectral range, in principle, can be made much higher than is possible with time-domain NIRS, without losing efficiency. In time-domain NIRS methods that use gating, improvement in resolution comes at the cost of reduced efficiency.

By analogy, for a rapidly tunable or swept laser, the instantaneous coherence time (or length), inversely proportional to the instantaneous linewidth, defines the range of time delays (or path delays) that can be measured using iNIRS. The instantaneous linewidth, $\delta\nu$, is defined by the time scale of random phase fluctuations during the frequency sweep [62]. Specifically, a function describing the roll-off of the iNIRS signal, $I_s^{(\text{iNIRS})}(\mathbf{r}, \tau_s)$, over the measurement range, $\phi(\tau_s)$, can be defined. This function has a maximum at a time delay of zero between the reference and sample arms, and decreases for positive or negative time delays [Fig. 5(b)]. Assuming that $\phi(\tau_s)$ has a Gaussian shape [cf. Eq. (30)], and that the TOF measurement range τ_c is the delay at which $\phi(\tau_s) = \frac{1}{2}\phi(0)$, τ_c can be written as

$$\tau_c = \frac{4\ln(2)}{\pi\delta\nu} = \frac{4\ln(2)}{\pi} \frac{\lambda_c^2}{\nu\delta\lambda}, \quad (33)$$

where $\delta\lambda = \lambda_c^2\delta\nu/\nu$ is the instantaneous laser linewidth.

Equation (31) and Eq. (33) show that the performance of the iNIRS system strongly depends on the tuning parameters of the light source. The spectral bandwidth determines TOF resolution, while the spectral linewidth determines the TOF measurement range (or coherence time). The relationship between $\delta\tau_{s,l}$, τ_c , and coherence properties of the light source are summarized in Fig. 5.

In iNIRS, since the laser wavelength is changed over time, any filtering of the temporal signal will act as a filter of optical frequency. Thus, the TOF measurement range of the iNIRS signal is also limited by the detector bandwidth. This can be addressed similarly to the effect of finite linewidth, i.e. by incorporating detector frequency response into the function $\phi(\tau_s)$. At the tuning speeds, ranges, and τ_s values used in this study, we measured $\phi(\tau_s)$ to vary by $< 4\%$ over the TOF range of interest. Moreover, correcting our data for the roll-off resulted in negligible changes in fitted optical properties for this study.

Relations (31) and (33) can be now used to estimate the laser parameters required to achieve the TOF resolution and range appropriate for analyzing the DTOF in a turbid medium under specific source-detector separation. In particular, $\rho = 3$ cm requires a range of $\tau_c = 5$ ns. To achieve this measurement range, the iNIRS system would require an instantaneous linewidth

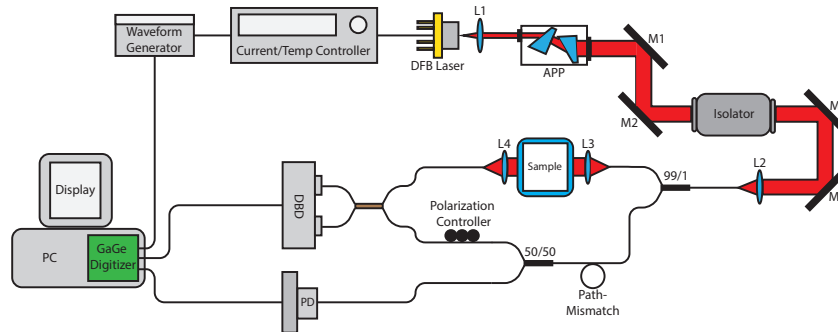


Fig. 6. Layout of the iNIRS optical system. The waveform generator sinusoidally modulates the current (with repetition frequency $f_r = 50$ kHz) supplied by the current controller which drives the DFB laser. The frequency-swept near infrared light is collimated by an aspheric lens (L1) and the shape of the beam is changed from elliptical to circular as it passes through the anamorphic prism pair (APP). Mirrors M1 and M2 are used to level the beam with the optical table and guide it through the isolator. Mirrors M3 and M4 serve to couple the beam through lens L2 into the single mode fiber. The beam is then divided into reference and sample arms (1% and 99% respectively) via a 99/1 fiber coupler. The beam in the sample arm is collimated with lens L3 and irradiates the sample. The scattered light from the sample is collected by L4 and fiber coupled. The light in the reference arm undergoes a path delay and is then split into two arms with a 50/50 fiber coupler, where one arm is detected by a photodetector (PD) to monitor power and the other arm passes through a polarization controller. The reference and sample arms are finally combined by the 50/50 fiber coupler and the resulting interference pattern is detected by a dual balanced detector (DBD), digitized with a GaGe digitizer, then stored and processed by the PC.

of $\delta\lambda = 0.57$ pm ($\delta\nu = 176.51$ MHz). To achieve a TOF resolution of 10 – 100 ps, the iNIRS system would require a bandwidth $\Delta\lambda$ of 28.5 – 285.5 pm ($\Delta\nu$ of 8 – 88 GHz), assuming a central wavelength of $\lambda_c = 855$ nm and $\nu = 0.226$ mm/ps.

Notably, due to the intrinsic temporal blurring of the scattering process, extended TOF resolution provides little additional information about DTOF beyond a certain threshold that depends on the source-detector separation. Hence, the bandwidth to linewidth ratio is 50 – 500 in the above example, but could be as low as 10 if the requirement on the bandwidth is relaxed for large source-detector separations.

3. Experimental setup

The optical system is depicted in Fig. 6. Light from a distributed feedback (DFB) [63] tunable light source (Eagleyard EYP-DFB-0855-00150-1500-TOC03) with central wavelength $\lambda_c = 855$ nm and a static linewidth of 2 MHz FWHM (full-width at half maximum of the power spectrum) is collimated using a Thorlabs aspheric lens. Then, the light beam passes through an anamorphic prism pair with $2.5\times$ magnification, which converted the elliptical shape of the laser output beam into a nearly circular shape. Subsequently, the beam is directed using mirrors through a 55 dB optical isolator (Thorlabs IOT-5-850-VLP) in order to minimize the feedback caused by back-reflections from ferrule angle polished (FC/APC) fiber connectors. FC/APC connectors reflect approximately -55 dB of light back into the laser cavity. If no isolator is used, such feedback has a negative impact on the DFB laser operation and may lead to mode hopping. The resulting beam is focused to a single mode fiber using horizontal and vertical mirror-based adjustments. Subsequently, the light beam is divided into the sample and reference

arms via a 99/1 fiber coupler (99% sample and 1% reference). The sample arm light is then collimated using another Thorlabs aspheric lens and illuminates the liquid phantoms at normal incidence while another collimated (Thorlabs aspheric lens) single mode fiber collects the light transmitted through the sample. The reference light, after being sampled with an additional coupler and photodiode, passes through a polarization controller and is interfered with the light in the sample arm using a 50/50 fiber coupler.

The temperature as well as the current controlling the laser operation are regulated using a laser diode current driver with integrated temperature controller and analog current modulation capability (Newport LDC-3724C). The wavelength of the DFB laser is tuned in time by modulating the input current using a sinusoidal waveform of frequency $f_r = 50$ kHz. This waveform is generated by a programmable function generator (Stanford Research DS 345). Therefore, the laser wavelength is swept bidirectionally, so the effective laser tuning rate is $f_t = 100$ kHz. However, due to possible differences between signals generated using both wavelength sweep directions, we subsequently use the forward laser sweeps (from shorter to longer wavelengths) only. Due to the fact that only forward sweeps were used, the measurement time interval is equal to twice the sweep time. The use of both wavelength sweep directions may require additional signal processing to compensate for eventual differences in power and noise levels.

Finally, the spectral interference signal is detected by a dual-balanced photoreceiver (New Focus 1807-FS). It consists of two photodiodes, which register the spectral fringes with a π phase shift between them. Subsequently, the signals are subtracted by a differential amplifier such that the resulting signal approximates the real part of the cross-spectral density function $\mathcal{W}_{rs}(\mathbf{r}, \nu)$ [see Eq. (2)]. This signal is then acquired using a high speed digitizer (GaGe PCIe CSE1442). From now on the \mathbf{r} -dependence of the measured and theoretical functions will be omitted since the geometry is fixed.

4. Signal processing

The signal acquired using the setup described above is subsequently processed in order to convert the cross-spectral density function to the sample field autocorrelation, $\Gamma_{rs}^{(iNIRS)}(\tau_s)$, using Eq. (4). This digital signal processing procedure consists of the following steps. Firstly, due to the nonlinear (sinusoidal) sweep of the laser, and to a lesser extent, the nonlinear relation between wavelength and optical frequency ν , the fringe pattern needs to be remapped such that points of the acquired signal are equidistantly spaced in the ν -domain rather than in the time-domain. For this purpose one first determines the phase of the fringes acquired without a sample in the interferometer sample arm by using the Hilbert transformation. Subsequently, the phase of the resulting function (proportional to ν) is fitted to a polynomial, which relates the signals in the time- and ν -domains. This polynomial is then used to interpolate each fringe pattern such that the oscillations are equidistant in the optical frequency domain [as in Fig. 4(c)]. Secondly, after compensating for the phase nonlinearity, the signal is zero-padded, windowed using a Hamming function and inverse Fourier transformed using a Fast Fourier Transform algorithm.

The set of N processed signals, i.e. $\left\{ \hat{\Gamma}_{rs}^{(iNIRS)}(\tau_s, n \times t_m) \right\}_{n=0}^{N-1}$, with t_m denoting the measurement time interval, is then used to calculate the photon time-of-flight in the sample using the following expression:

$$\hat{I}_s^{(iNIRS)}(\tau_s) = \frac{1}{N} \sum_{n=0}^{N-1} \hat{I}_s^{(iNIRS)}(\tau_s, n \times t_m), \quad (34)$$

where instantaneous intensity signals are given by

$$\hat{I}_s^{(\text{iNIRS})}(\tau_s, n \times t_m) = \left| \hat{\Gamma}_{rs}^{(\text{iNIRS})}(\tau_s, n \times t_m) \right|^2.$$

In order to account for the noise from the interferometer reference arm and detection electronics, a set of background signals, acquired with a blocked sample arm, are processed in an identical fashion. This procedure yields the background intensity, $\hat{I}_{bg}^{(\text{iNIRS})}(\tau_s)$, which is subtracted from $\hat{I}_s^{(\text{iNIRS})}(\tau_s)$ to get the estimated, noise-bias-corrected DTOF, $\tilde{I}_s^{(\text{iNIRS})}(\tau_s)$:

$$\tilde{I}_s^{(\text{iNIRS})}(\tau_s) = \hat{I}_s^{(\text{iNIRS})}(\tau_s) - \hat{I}_{bg}^{(\text{iNIRS})}(\tau_s),$$

from which any negative values are excluded from further analysis.

Instantaneous intensity signals, $\hat{I}_s^{(\text{iNIRS})}(\tau_s, n \times t_m)$ are then exploited to calculate the normalized intensity autocorrelation function using the following estimator:

$$\hat{g}_2^{(\text{iNIRS})}(\tau_s, \tau_d) = \frac{1}{(N-m) \left[\tilde{I}_s^{(\text{iNIRS})}(\tau_s) \right]^2} \sum_{k=0}^{N-m-1} \tilde{I}_s^{(\text{iNIRS})}(\tau_s, k \times t_m) \tilde{I}_s^{(\text{iNIRS})}(\tau_s, k \times t_m + \tau_d), \quad (35)$$

where $\tilde{I}_s^{(\text{iNIRS})}(\tau_s, n \times t_m) = \hat{I}_s^{(\text{iNIRS})}(\tau_s, n \times t_m) - \hat{I}_{bg}^{(\text{iNIRS})}(\tau_s)$ and m is the maximum lag index, which was set to 100. Furthermore, $\tau_d = i \times t_m$, where $i = 0, 1, \dots, m$, stands for the autocorrelation time lag.

The noise-bias-corrected intensity autocorrelation function, $\tilde{g}_2^{(\text{iNIRS})}(\tau_s, \tau_d)$ is calculated using the following procedure. Firstly, values of the function $\hat{g}_2^{(\text{iNIRS})}(\tau_s, \tau_d)$ which are below the noise level are determined. These points as well as the zero-lag point are further excluded from fits to DWS theory.

Accurate comparison between experimental and theoretical data requires an appropriate time reference. In diffusion theory, time-of-flight is taken with respect to the moment at which the light pulse was injected to the sample. Thus, the experimentally measured time-of-flight should also include the photon traversal time through the cuvette filled with water, τ_w [64]. For the experimental setup described in section 3, $\tau_w = 44.33$ ps. All experimental data are displayed assuming that the light pulse is injected into the sample at $\tau_s = 0$; thus, τ_s represents the time-of-flight in the scattering medium.

5. Results

Twenty phantoms were prepared by mixing increasing volumes (50 – 1000 μL in steps of 50 μL) of Intralipid 20% ($\mu'_s = 170.3 \text{ cm}^{-1}$ at $\lambda = 855 \text{ nm}$ [65], $\mu'_s = 184 \text{ cm}^{-1}$, $\mu_a = 0.0351 \text{ cm}^{-1}$ at $\lambda = 833 \text{ nm}$ [66]) in a glass cuvette containing 2 mL of deionized water. These fluid phantoms were then placed in the sample arm. For each sample, $N = 40,000$ consecutive interference signals were acquired at a laser sweep rate of 100 kHz and tuning range $\Delta\nu$ of 10.5 GHz, for which the time-resolution, $\delta\tau_{s,I_s}$ is 60 ps FWHM. The recorded fringe patterns were processed separately and then averaged in order to increase the signal-to-noise ratio [cf. Eq. (34)]. The resulting photon distributions of time-of-flight under varying concentrations of Intralipid 20% (c) are depicted in Fig. 7. It follows that the averaged photon time-of-flight,

$$\bar{\tau}_s^{(\text{iNIRS})} = \frac{\int_{-\infty}^{\infty} \tau_s \tilde{I}_s^{(\text{iNIRS})}(\tau_s) d\tau_s}{\int_{-\infty}^{\infty} \tilde{I}_s^{(\text{iNIRS})}(\tau_s) d\tau_s}$$

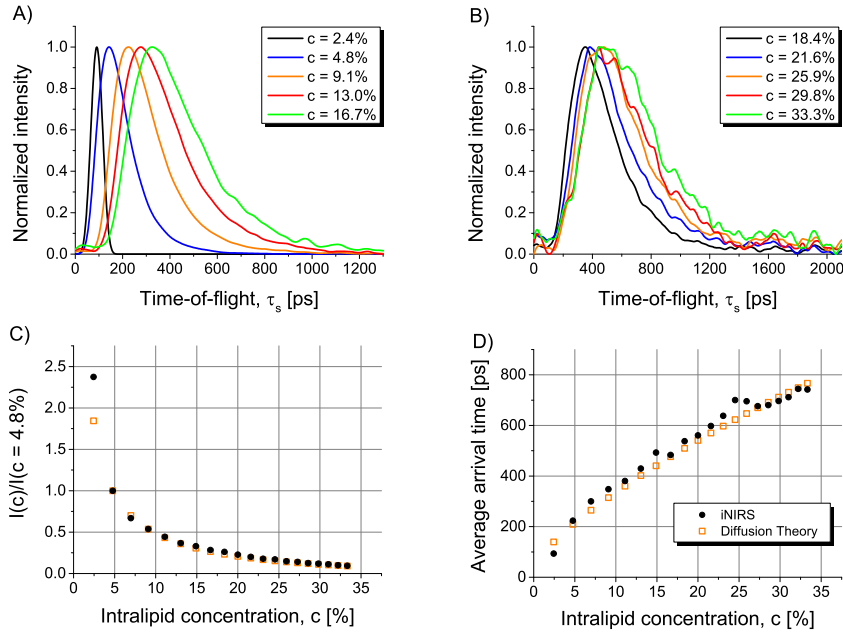


Fig. 7. (A,B) Photon time-of-flight distribution under varying concentrations of Intralipid 20%, denoted by c . As the Intralipid 20% concentration is increased, the time-integrated intensity signal is attenuated (C), and the mean arrival time is increased (D). Theoretical points in subfigures C and D were obtained using Eq. (26) and the values of $\mu_a = 4.53 \times 10^{-2} \text{ cm}^{-1}$ (water absorption due to negligible lipid absorption at near-infrared wavelengths) and $\mu'_s(c) = c\mu'_{s,t}$, where $\mu'_{s,t} = 170.27 \text{ cm}^{-1}$ is theoretical estimation of the reduced scattering coefficient of Intralipid 20% [65]. The attenuation plots are normalized with respect to $c = 4.8\%$, since the diffusion approximation is invalid for smaller concentrations.

increases with increasing c , which is due to increasing sample optical thickness, $L\mu'_s(c)$. Furthermore, as predicted by time-resolved diffusion theory, the photon time-of-flight distribution curves are broadened and attenuated with increasing concentration.

For the experimental geometry depicted in Fig. 6, measured photon DTOFs can be fitted to Eq. (26) with $\rho = 0$, $L = 1 \text{ cm}$, $n = 1.33$ and experimentally determined values of $\sigma_d^2 = 0.09 \text{ mm}^2$ and $\sigma_s^2 = 0.04 \text{ mm}^2$ for the incident beam width of $500 \mu\text{m}$. Such nonlinear fitting was performed by minimizing the squared norm of the difference between transmittance $I_s^{(\text{DE})}(\tau_s)$ resulting from diffusion theory [Eq. (26)] and experimental data, $\tilde{I}_s^{(\text{iNIRS})}(\tau_s)$, namely by solving the following optimization problem:

$$\min_{(\mu_a, \mu'_s)} \left\| \log \left[I_s^{(\text{DE})}(\tau_s) * I_0(\tau_s) \right] - \log \left[\alpha \tilde{I}_s^{(\text{iNIRS})}(\tau_s) \right] \right\|^2, \quad (36)$$

where α is a normalization factor which accounts for the arbitrary height of the measured intensity. The absorption coefficient determines the slope of the DTOF for large values of τ_s [2]. Therefore, the optimization procedure [Eq. (36)] is performed on a logarithmic scale such that the absorption term, $(\exp[-\mu_a \nu \tau_s])$ in Eq. (26) as well as the multiplicative speckle noise, become additive. Moreover, the limited TOF resolution broadens the experimentally determined DTOF [cf. Eq. (32)]. In order to include this effect in the theoretical model we convolve $I_s^{(\text{DE})}(\tau_s)$ with the instrument response function before fitting. The IRF is measured for a cuvette

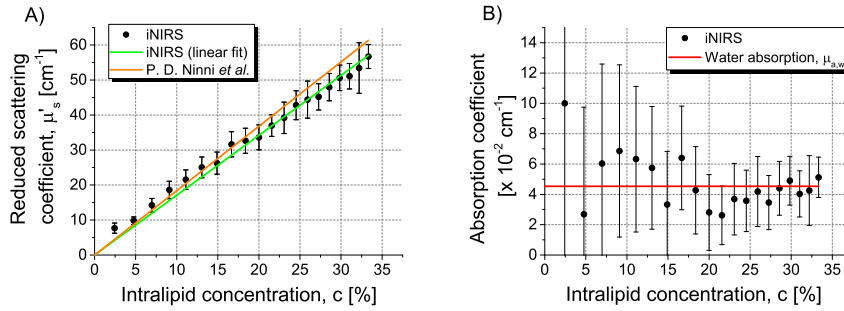


Fig. 8. Optical properties determined by iNIRS in fluid tissue phantoms with varying Intralipid 20% concentrations, c : μ'_s (A), μ_a (B). Reduced scattering coefficients are compared to data reported in [66] by assuming a linear dependence of μ'_s on c (orange line in subfigure A). Furthermore in subfigure A, the green solid line depicts a linear fit to the experimental data, i.e., $\mu'_s(c) = \eta c$ with $\eta = 171.19 \pm 1.92 \text{ cm}^{-1}$. The error bars denote the standard errors of the extracted parameter values.

filled with deionized water only, i.e. when $c = 0\%$ and the a time shift was applied to the IRF to center it at the origin, while all iNIRS DTOFs were shifted by τ_w less than this time shift.

The optical properties resulting from the above procedure are depicted in Fig. 8, while selected individual DTOFs compared with those predicted by Eq. (26) are given in Fig. 9. For low concentrations of Intralipid 20%, the phantom's optical thickness is much less than 10. Therefore the predictions of the diffusion approximation to the RTE are incorrect and significant deviation from this theory can be noticed. However, for larger values of c , the diffusion approximation is satisfied ($L\mu'_s \geq 10$ transport mean free paths) and experimental data agrees very well with Eq. (26). Therefore, the values of μ'_s and μ_a obtained for $c = 2.4\%$ are excluded from further analysis.

It should be pointed out that the agreement between theoretically and experimentally determined TOF distributions improves with increasing c . However, the disagreement is noticeable for very early photons, and may be anisotropy dependent [67]. The limitations of diffusion theory aside, errors in the bias subtraction are also apparent at high concentrations.

For $c \geq 4.8\%$, values of the reduced scattering coefficient increase almost linearly with increasing c . Dependent scattering effects [43] and changes in the effective refractive index are expected at much higher concentrations. Accordingly, we can assume that μ'_s is a linear function of c for all phantoms, such that the values of $\mu'_s(c)$ can be extrapolated for larger concentrations of Intralipid 20%. In particular, for $c = 100\%$, we obtain $\mu'_s = 171.19 \pm 1.92 \text{ cm}^{-1}$.

On the other hand, the values of the absorption coefficients are fairly constant, with an average value of $\mu_a = (4.73 \pm 1.78) \times 10^{-2} \text{ cm}^{-1}$. This is explained by the fact that the $\mu_{a,w}$ of water at $\lambda = 855 \text{ nm}$ is $\mu_{a,w} = 4.53 \times 10^{-2} \text{ cm}^{-1}$, while the absorption of Intralipid 20% is negligible [65]. The standard error of the absorption coefficient μ_a significantly decreases for $c \geq 20\%$, coinciding with improved agreement between diffusion theory and experimental data for large values of τ_s (slope of the TOF distribution).

The extracted values of μ'_s and μ_a are compared with other measurements and theoretical predictions in Table 1. In general, the value of μ'_s , determined here is slightly smaller than those determined from other measurements but agrees very well with theoretical estimations given in [65]. The small disagreement with other studies may be due in part to the use of a longer wavelength in this study. Further differences may result from assumptions pertaining to boundary conditions and experimental geometry (transmission or reflectance).

Note that for $c = 33.1\%$, $\mu'_s \approx 55 \text{ cm}^{-1}$. Thus, for a cuvette of length $L = 1 \text{ cm}$, the optical

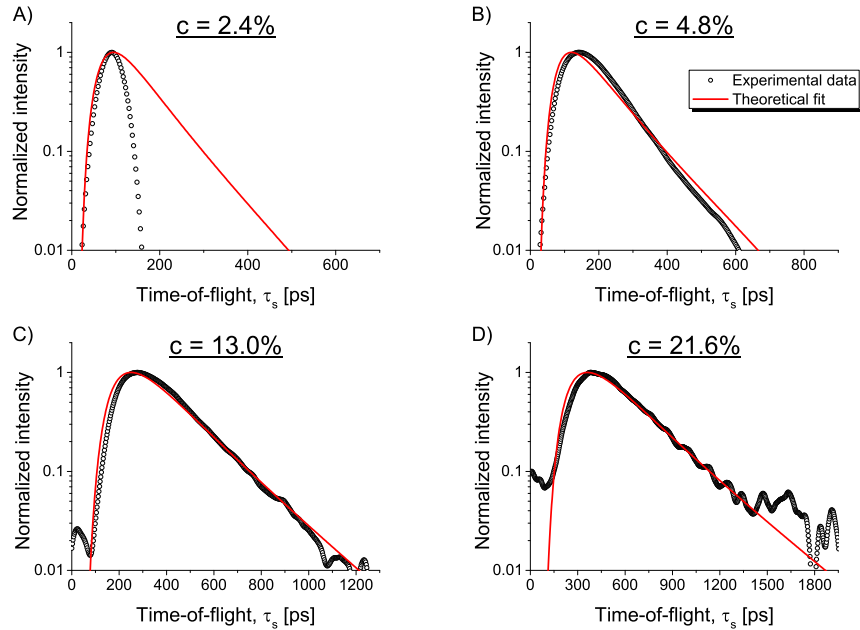


Fig. 9. Diffusion theory validation. Plots depict the experimental transmittance and fits to diffusion theory [cf. Eq. (26)] under varying Intralipid 20% concentrations: (A) $c = 2.4\%$, (B) $c = 4.8\%$, (C) $c = 13.0\%$, and (D) $c = 21.6\%$. For low concentrations ($c < 4.8\%$) significant deviations from the diffusion approximation are noticed. For $c \geq 4.8\%$ diffusion theory agrees well with experimental data. The mean squared error, MSE for each fit, after thresholding normalized intensity values below 0.08, is: (A) $MSE = 0.448$, (B) $MSE = 0.050$, (C) $MSE = 0.054$, and (D) $MSE = 0.038$.

Table 1. Comparison of optical properties determined by iNIRS with literature values.

μ'_s [cm^{-1}]	μ_a [$\times 10^{-2} \text{ cm}^{-1}$]	Reference	Remarks
178.6 ± 5.4	9.0 ± 2.0	[29]	Intralipid 20% mixed with India Ink, $\lambda = 763 \text{ nm}$
180.0	6.8 ± 0.3	[30]	Standard error for μ'_s is not reported, $\lambda = 852 \text{ nm}$
184.0 ± 2.6	3.51 ± 0.02	[66]	$\lambda = 833 \text{ nm}$
187.0 ± 1.7	—	[68]	$\lambda = 830 \text{ nm}$
170.3	—	[65]	Theoretical estimation, $\lambda = 855 \text{ nm}$
171.19 ± 1.92	4.73 ± 1.78	iNIRS	$\lambda = 855 \text{ nm}$

thickness is roughly 55 transport mean free paths, which assuming a scattering anisotropy factor of $g = 0.53$ [65], corresponds to around 117 scattering events. This shows that iNIRS is capable of determining optical properties of highly scattering media.

The set of N acquired DTOF intensity signals for the fluid phantom with $c = 4.8\%$ was also used to calculate the normalized intensity autocorrelation function, $\tilde{g}_2^{(\text{iNIRS})}(\tau_s, \tau_d)$. The estimated intensity autocorrelation function is subsequently exploited to calculate the absolute value of the field autocorrelation function $\tilde{g}_1^{(\text{iNIRS})}(\tau_s, \tau_d)$ using expression (23). The value of

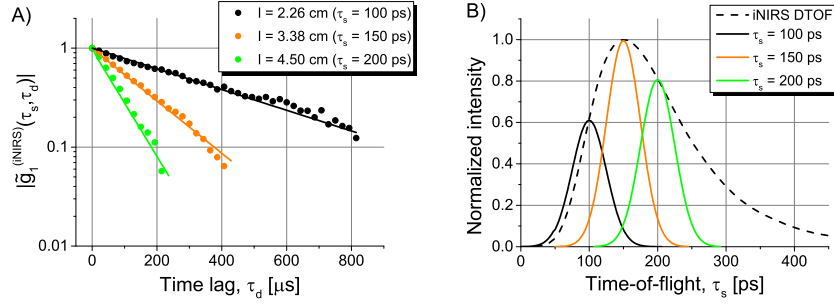


Fig. 10. Time-of-flight-resolved scatterer dynamics. (A) The absolute value of the field autocorrelation function, $|\hat{g}_1^{(iNIRS)}(\tau_s, \tau_d)|$, obtained from the temporal intensity autocorrelation $\hat{g}_2^{(iNIRS)}(\tau_s, \tau_d)$ using Eq. (23), is plotted for three different path lengths ($l = v\tau_s$), corresponding to time-of-flight values, τ_s , and TOF windows marked on the iNIRS DTOF (B). The solid lines in subfigure A denote the fits of the experimental normalized field autocorrelation function to the exponential decay predicted by DWS theory [cf. Eq. (27)].

the β parameter was first calculated from $\hat{g}_2^{(iNIRS)}(\tau_s, \tau_d)$ using Eq. (24). For the experimental setup depicted in Fig. 6 we obtained an average value of $\beta = 0.985 \pm 0.031$.

The resulting values of the first-order field autocorrelation function are plotted in Fig. 10(a) for three different values of l , which are marked together with TOF resolution ($\delta\tau_{s,l_s} \approx 60$ ps FWHM) on the corresponding iNIRS DTOF in Fig. 10(b). Figure 10(a) also presents the fits of DWS theory to the experimental data. Specifically, the squared norm difference between theoretical function, $|g_1^{(DWS)}(\tau_s, \tau_d)|$, resulting from Eq. (27) and experimentally determined values of the function $\hat{g}_1^{(iNIRS)}(\tau_s, \tau_d)$, was minimized:

$$\min_{\xi} \left\| \left| g_1^{(DWS)}(\tau_s, \tau_d) \right| - \left| \hat{g}_1^{(iNIRS)}(\tau_s, \tau_d) \right| \right\|^2, \quad (37)$$

where $\xi = 2k^2 D_B \mu'_s v \tau_s$.

Results presented in Fig. 10(a) further show that the decay rate, ξ , of the normalized intensity autocorrelation function increases with increasing photon path length l , which means that the photons traveling longer path lengths decorrelate faster than early photons. Photons with long paths decorrelate faster since they experience more scattering and cumulative momentum transfer in the DWS framework.

Figure 11 depicts the decay rate ξ of the first-order field autocorrelation function (extracted from the intensity autocorrelation function using Siegert relation [Eq. (23)]) under increasing values of τ_s . These experimental results are compared with predictions of DWS theory, which assumes a linear increase of ξ proportional to the number of reduced scattering events. The fit to DWS theory is applied for $\tau_s > 200$ ps, due to the fact that earlier photons experience less momentum transfer than is expected from DWS theory. From this analysis and using experimentally determined value of μ'_s we obtained a Brownian diffusion coefficient, i.e., $D_B = (2.23 \pm 0.15) \times 10^{-12} \text{ m}^2\text{s}^{-1}$. This value agrees well with data reported in [30]: $D_B = (1.9 \pm 0.2) \times 10^{-12} \text{ m}^2\text{s}^{-1}$ and in [69]: $D_B = (1.6 \pm 0.2) \times 10^{-12} \text{ m}^2\text{s}^{-1}$, but is smaller than theoretical estimation of $D_B = 3.6 \times 10^{-12} \text{ m}^2\text{s}^{-1}$ [30].

In summary, the experimental results show that iNIRS is capable of simultaneously extracting the optical properties and dynamics of the turbid medium.

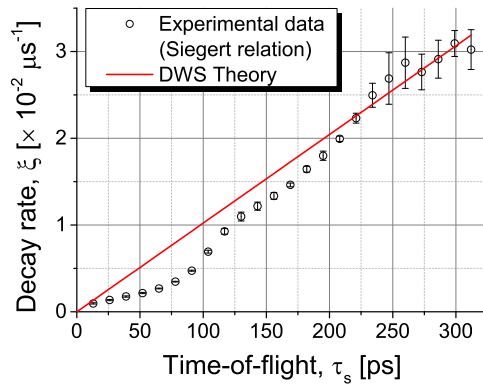


Fig. 11. Diffusing wave spectroscopy validation. The decay rate, ξ of the first-order auto-correlation function, extracted from intensity autocorrelation function using Siegert relation [Eq. (23)], is plotted for increasing values of τ_s and fit assuming a linear dependence of ξ on τ_s for $\tau_s > 200$ ps, as predicted by DWS theory ($\xi(\tau_s) = 1.02 \times 10^{-4} \tau_s$). The error bars denote the standard error of ξ extracted by fitting experimental data using Eq. (27) and Eq. (37). The time-of-flight through a water-filled cuvette is $\tau_w = 44.33$ ps.

6. Summary and discussion

We have introduced interferometric near-infrared spectroscopy, which simultaneously derives the optical properties and dynamics of a turbid medium from analysis of the spectral interference fringe pattern. We described a procedure to determine the distribution of the photon time-of-flight from the spectral interference fringes. Moreover, we directly related iNIRS intensity fluctuations to theoretical descriptions of time-of-flight resolved autocorrelations provided by time-resolved diffusion theory and diffusing wave spectroscopy. Therefore, iNIRS achieves the functionality of a hybrid FD NIRS/DCS instrument with a single modality.

Next, the interferometric setup, which was described in detail, was used to measure the spectral fringe pattern. This signal, after digital processing, was subsequently used to extract the optical and dynamical properties of fluid phantoms that mimic biological tissue. Optical and dynamical properties of turbid media were determined from the experimental data by using diffusion theories [Eq. (26) and Eq. (27)]. For source-detector separations or time-of-flight regimes where diffusion theory is not valid, light propagation in a turbid medium can be modeled using Monte Carlo simulations [70].

The performance of the iNIRS system strongly depends on the spectral and tuning parameters of the light source. For the reasons described in section 2.5, the spectral linewidth determines the TOF range, τ_c , while the bandwidth determines the TOF resolution, $\delta\tau_s$. It should be emphasized that the optical field autocorrelation function can be measured using the interferometer as long as the total TOF mismatch between the two interferometer arms is less than τ_c . However, simply increasing τ_c , by decreasing the laser linewidth, does not enable measuring the DTOF in an arbitrary turbid medium. This is due to the fact that the probability of detecting a photon emerging from the scattering medium decreases with increasing source-detector separation and also with increasing values of the absorption and scattering coefficients [Eq. (26)].

In section 2.2, it was determined that the analysis of the dynamics in a turbid medium requires rapidly tunable lasers. However, increasing the tuning rate of the light source reduces the TOF range, τ_c , due to laser tuning dynamics [61]. Nevertheless, the temporal resolution of the intensity autocorrelation function can be improved by a factor of two if both forward and

backward laser sweeps are used. In this study, only the interferometric signal acquired during the forward laser sweep was analyzed.

The iNIRS system can also be adapted to operate in reflectance geometry, which in some cases is the only possible way of examining biological tissue *in vivo*. This would require modifications to the optical setup as well as theoretical model for time-resolved reflectance [7, 57]. Measurements of the optical properties and dynamics of turbid media in reflectance geometry will be the subject of further studies.

7. Conclusions

We developed interferometric near-infrared spectroscopy, which simultaneously quantifies optical and dynamical properties of turbid media. This is achieved by using a rapidly-acquired series of spectral interference fringe patterns to determine both path-length-resolved intensities and their autocorrelations. We prove this by measuring both intensity and autocorrelation of light transmitted through diffusive fluid phantoms. There are two main benefits of our technique. Firstly, it achieves photon time-of-flight measurements more simply and cost-effectively than time-domain NIRS, without requiring pulsed lasers and time-correlated single photon counting devices. Secondly, the method significantly improves upon DCS by providing the capability to measure TOF-resolved intensity autocorrelation functions, from which scatterer dynamics can be readily quantified. The ultimate goal for this project is to apply this method to design an iNIRS device for real-time, *in vivo* functional analysis of human tissue.

Acknowledgment

We acknowledge support from the National Institutes of Health (R00NS067050, R01NS094681, P30AG010129). DB is supported by the Polish Ministry of Science within the Mobility Plus project (decision no. 1106/MOB/2013/0). We would like to thank Michael Radunsky and Ben Luey from Vescent Photonics Inc for useful technical advice.